INTERNATIONAL JOURNAL FOR NUMERICAL METHODS IN FLUIDS
Int. J. Numer. Meth. Fluids 2015; **78**:355–383
Published online 9 April 2015 in Wiley Online Library (wileyonlinelibrary.com). DOI: 10.1002/fld.4023

Well-balanced positivity preserving central-upwind scheme for the shallow water system with friction terms

A. Chertock[1], S. Cui[2], A. Kurganov[2,*,†] and T. Wu[2]

[1]*Department of Mathematics, NC State University, Raleigh, NC 27695, USA*
[2]*Mathematics Department, Tulane University, New Orleans, LA 70118, USA*

SUMMARY

Shallow water models are widely used to describe and study free-surface water flow. While in some practical applications the bottom friction does not have much influence on the solutions, there are still many applications, where the bottom friction is important. In particular, the friction terms will play a significant role when the depth of the water is very small. In this paper, we study shallow water equations with friction terms and develop a semi-discrete second-order central-upwind scheme that is capable of exactly preserving physically relevant steady states and maintaining the positivity of the water depth. The presence of the friction terms increases the level of complexity in numerical simulations as the underlying semi-discrete system becomes stiff when the water depth is small. We therefore implement an efficient semi-implicit Runge-Kutta time integration method that sustains the well-balanced and sign preserving properties of the semi-discrete scheme. We test the designed method on a number of one-dimensional and two-dimensional examples that demonstrate robustness and high resolution of the proposed numerical approach. The data in the last numerical example correspond to the laboratory experiments reported in [L. Cea, M. Garrido, and J. Puertas, Journal of Hydrology, 382 (2010), pp. 88–102], designed to mimic the rain water drainage in urban areas containing houses. Since the rain water depth is typically several orders of magnitude smaller than the height of the houses, we develop a special technique, which helps to achieve a remarkable agreement between the numerical and experimental results. Copyright © 2015 John Wiley & Sons, Ltd.

Received 30 December 2013; Revised 29 January 2015; Accepted 15 February 2015

KEY WORDS: shallow water equations with friction terms; central-upwind scheme; well-balanced scheme

1. INTRODUCTION

Shallow water equations are a set of hyperbolic partial differential equations derived by a vertical integration of Navier-Stokes equations. They are widely used in atmospheric sciences, oceanography, coastal engineering, and many other fields. In shallow water flow models, the horizontal length scale is considered to be much larger than the vertical one. As a result, the vertical effect can be neglected leading to a considerable simplification in the momentum equation, in which the vertical pressure gradients are replaced by the hydrostatic pressure. The simplest, yet commonly used, shallow water model is the Saint-Venant system [1], which in the two-dimensional (2-D) case reads

$$\begin{cases} h_t + (hu)_x + (hv)_y = R(x,y,t), \\ (hu)_t + \left(hu^2 + \dfrac{g}{2}h^2\right)_x + (huv)_y = -ghB_x, \\ (hv)_t + (huv)_x + \left(hv^2 + \dfrac{g}{2}h^2\right)_y = -ghB_y. \end{cases} \tag{1.1}$$

*Correspondence to: A. Kurganov, Mathematics Department, Tulane University, New Orleans, LA 70118, USA.
†E-mail: kurganov@math.tulane.edu

Here, $h(x,y,t)$ is the water depth, $u(x,y,t)$ and $v(x,y,t)$ are the x-component and y-component of the average velocity, $R(x,y,t)$ is the water source term, $B(x,y)$ is a function describing the bottom topography, and g is the gravity constant.

Solving the shallow water system numerically is a challenging task because of several reasons. First, many physically relevant solutions of (1.1) are small perturbations of steady states, characterized by a delicate balance between the flux and source terms. If the method does not accurately respect this balance, the numerical errors (which cannot be made too small on practically relevant grids) may lead to oscillations, in which the magnitude of artificial waves may be larger than the magnitude of the solution itself. The second major difficulty is related to the computation of solutions when the water depth h is very small or even zero. In such a case, small numerical oscillations may lead to appearance of negative values of h, which in turn would make it impossible to evaluate the eigenvalues of the system (1.1), which are $u \pm \sqrt{gh}$ and $v \pm \sqrt{gh}$.

A good numerical method for the system (1.1) should thus be well-balanced (in the sense that it must exactly preserve physically relevant steady states) and positivity preserving (in the sense that the computed values of h must be positive). In the past two decades, many well-balanced schemes have been developed (e.g., [2–17]). Some of them preserve only 'lake at rest' steady states, that is, $u \equiv v \equiv 0$, $h + B \equiv$ constant, [2–10, 12, 13], other can preserve a nonflat steady-state solution as well, [11, 15–17]. There are also well-balanced schemes that preserve the positivity of h (e.g., [2–6, 8, 9, 12, 13]).

In this paper, we focus on studying the effects of the bottom friction terms in the shallow water model, and thus, we consider the following modified version of (1.1):

$$\begin{cases} h_t + (hu)_x + (hv)_y = R(x,y,t), \\ (hu)_t + \left(hu^2 + \dfrac{g}{2}h^2\right)_x + (huv)_y = -ghB_x - \dfrac{\tau^x}{\rho}, \\ (hv)_t + (huv)_x + \left(hv^2 + \dfrac{g}{2}h^2\right)_y = -ghB_y - \dfrac{\tau^y}{\rho}, \end{cases} \tag{1.2}$$

where τ^x and τ^y are the two components of the bottom friction and ρ is the water density. The friction terms are computed by using the following formulae:

$$\frac{\tau^x}{\rho} = ghI^x, \qquad \frac{\tau^y}{\rho} = ghI^y, \tag{1.3}$$

where the I^x and I^y are the components of the bottom friction slope. There are many ways to model friction terms, e.g. [18, 19]. In this paper, we focus on the classical Manning formulation (e.g., [20–23]):

$$I^x = \frac{n^2}{h^{4/3}}\, u\sqrt{u^2+v^2}, \qquad I^y = \frac{n^2}{h^{4/3}}\, v\sqrt{u^2+v^2}, \tag{1.4}$$

where n is the Manning coefficient. Notice that if $h \approx 0$, the friction term (1.4) becomes a stiff damping term, which increases the level of complexity in the development of efficient numerical methods for the system (1.2).

The system (1.2) still admits 'lake at rest' steady states. However, we are interested in simulating drainage of the rain water in urban areas. In such situations, the simplest yet physically relevant quasi one-dimensional (1-D) steady-state solutions correspond to the case when the water flows over a slanted infinitely long surface with a constant slope as illustrated in Figure 1 (left). Such steady states (both 1-D and 2-D) are discussed in Section 2.

A well-balanced Roe-type numerical scheme that exactly preserves steady states shown in Figure 1 was proposed in [24]. However, to maintain the positivity of the water depth h, the scheme in [24] requires one to use very small time steps and thus may not be robust in certain settings. Another Godunov-type scheme for the 1-D version of (1.2) was proposed in [25]. Though this method does not suffer from restrictive time stepping, it is capable of preserving 'lake at rest' steady states only.

DOI: 10.1002/fld

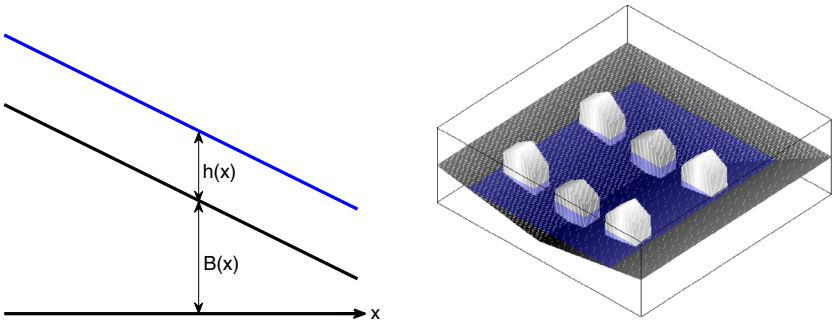

Figure 1. The bottom setting of numerical examples. The figure on the left corresponds to the quasi one-dimensional steady state. The figure on the right illustrates the case of urban draining with obstacles like houses. The slope of the bottom and the height of the houses are out of scale.

In this paper, we develop a central-upwind scheme for the system (1.2), which is well-balanced, positivity preserving, and efficient. Central-upwind schemes have been proposed for general hyperbolic system of conversation law in [26–29] and extended to the shallow water equations and related models in [8, 9, 30]. These schemes belong to the family of Godunov-type central schemes that are Riemann-problem-solver-free, robust, and highly accurate. The extension of central-upwind schemes to the shallow water systems with friction terms is very natural and it is described in both the 1-D (Section 3.1) and 2-D (Section 3.2) cases (the 2-D scheme presented here is restricted to Cartesian meshes). The efficiency of the proposed central-upwind scheme hinges on the use of an efficient second-order semi-implicit ODE solver we have recently developed in [31] and briefly describe in Section 3.3.

The designed scheme is tested in a number of numerical experiments including those with realistic urban bottom topography structures, schematically shown in Figure 1 (right). The results presented in Section 4 demonstrate the superb performance of the proposed numerical method. The data in Example 8 correspond to the laboratory experiments reported in [32], designed to mimic the rainwater drainage in urban areas containing houses. Since the rainwater depth is typically several orders of magnitude smaller than the height of the houses, the proposed central-upwind scheme has been modified to accurately handle such situations as follows. First, the houses are removed from the computational domain, which becomes a punctured domain with many internal solid wall boundary pieces. Second, the rainwater falling over the houses is redistributed to the areas near the edges of the houses. This helps to achieve a remarkable agreement between the numerical and experimental results.

2. STEADY-STATE SOLUTIONS

In this section, we discuss steady-state solutions of the shallow water system (1.2). We begin with the simplest 1-D case, in which the system (1.2) reduces to

$$\begin{cases} h_t + (hu)_x = R(x,t), \\ (hu)_t + \left(hu^2 + \dfrac{g}{2}h^2\right)_x = -ghB_x - g\dfrac{n^2}{h^{1/3}}|u|u. \end{cases} \tag{2.1}$$

In the situation when the water source is zero ($R \equiv 0$), the steady-state solution satisfies the time-independent system:

$$\begin{cases} (hu)_x = 0, \\ \left(hu^2 + \dfrac{g}{2}h^2\right)_x = -ghB_x - g\dfrac{n^2}{h^{1/3}}|u|u. \end{cases} \tag{2.2}$$

In general, this system is not solvable, but one can obtain a particular nontrivial ($u \neq 0$) steady state in the form

DOI: 10.1002/fld

$$hu \equiv \text{constant}, \quad h \equiv \text{constant}, \quad B_x \equiv \text{constant}. \tag{2.3}$$

This solution corresponds to the situation when the water flows over a slanted infinitely long surface with a constant slope. Indeed, if we assume that $B_x \equiv -C$, where $C > 0$ is a constant, and denote $hu \equiv q_0$, then the second equation of (2.2) can be rewritten as

$$\Big(-\frac{q_0^2}{h^2} + gh\Big)h_x = ghC - g\frac{n^2}{h^{1/3}}|u|u, \tag{2.4}$$

and one obtains

$$h \equiv h_0 = \left(\frac{n^2 q_0^2}{C}\right)^{3/10}, \quad hu \equiv q_0, \quad B_x \equiv -C, \tag{2.5}$$

where h_0 is the so-called normal depth. A simple analysis of the ODE (2.4) shows that this steady state is expected to be stable in the supercritical case, that is, when h_0 is below the critical depth h_c:

$$h_0 < h_c := \left(\frac{q_0}{g}\right)^{1/3}. \tag{2.6}$$

The structure of 2-D steady states is substantially more complicated. However, the quasi 1-D steady-state solutions

$$h \equiv \text{constant}, \quad hu \equiv \text{constant}, \quad hv \equiv 0, \quad B_x \equiv \text{constant}, \quad B_y \equiv 0, \tag{2.7}$$

or

$$h \equiv \text{constant}, \quad hu \equiv 0, \quad hv \equiv \text{constant}, \quad B_x \equiv 0, \quad B_y \equiv \text{constant} \tag{2.8}$$

are still physically relevant to the situation depicted in Figure 1.

In the next sections, we design both 1-D and 2-D central-upwind schemes that exactly preserve the aforementioned steady states (2.5) and (2.7), (2.8), respectively.

3. NUMERICAL METHOD

In this section, we present a well-balanced and positivity preserving semi-discrete central-upwind scheme for the shallow water equations with friction terms in both 1-D and 2-D. The scheme is derived along the lines of [9], and, therefore, here, we only describe its main components following the key ideas from [9]. In particular, the well-balanced property of the scheme will be ensured by a special finite-volume-type quadrature used for discretizing the geometric source term on the right-hand side of the system. We also introduce a new variable for the water surface $w := h + B$. As it has been shown in [9], working with w (rather than with h) is important for preserving 'lake at rest' steady states at the discrete level. Even though in this work, we focus on different types of steady states, described in Section 2, our goal is to design a numerical method, which preserves both the 'lake at rest' and steady states (2.5), (2.7), and (2.8). The positivity preserving property is achieved by the following: (i) replacing the bottom topography function B with its continuous piecewise linear (or bilinear in the 2-D case) approximation (done exactly the same way as in [9]); and (ii) a special positivity preserving correction of the piecewise linear reconstruction for the water surface w (which is different from the one proposed in [9]).

It should be observed that a successful implementation of the central-upwind scheme would be impossible without the use of an accurate and efficient time integration method that maintains the aforementioned important features of the semi-discrete scheme. In what follows, we first overview the 1-D and 2-D central-upwind schemes in Sections 3.1 and 3.2, respectively, and then, in Section 3.3, describe a new semi-implicit Runge-Kutta ODE solver we have recently developed in [31].

DOI: 10.1002/fld

3.1. One-dimensional central-upwind scheme

We start with a description of a well-balanced positivity preserving central-upwind scheme for the 1-D shallow water equations (2.1). We first rewrite the system (2.1) in an equivalent form in terms of $w := h + B$ and $q := hu$:

$$\begin{cases} w_t + q_x = R(x,t), \\ q_t + \left[\dfrac{q^2}{w-B} + \dfrac{g}{2}(w-B)^2\right]_x = -g(w-B)B_x - g\dfrac{n^2}{(w-B)^{7/3}}|q|q. \end{cases} \tag{3.1}$$

We use the notations

$$\boldsymbol{U} := \begin{pmatrix} w \\ q \end{pmatrix}, \ \boldsymbol{F}(\boldsymbol{U}, B) := \begin{pmatrix} q \\ \frac{q^2}{w-B} + \frac{g}{2}(w-B)^2 \end{pmatrix}$$

and

$$\boldsymbol{S}(\boldsymbol{U}, R, B) := \begin{pmatrix} R(x,t) \\ -g(w-B)B_x \end{pmatrix}, \quad \boldsymbol{M}(\boldsymbol{U}, B) := \begin{pmatrix} 0 \\ -g\frac{n^2}{(w-B)^{7/3}}|q|q \end{pmatrix},$$

so that the system of balance laws (3.1) takes the following vector form:

$$\boldsymbol{U}_t + \boldsymbol{F}(\boldsymbol{U}, B)_x = \boldsymbol{S}(\boldsymbol{U}, R, B) + \boldsymbol{M}(\boldsymbol{U}, B). \tag{3.2}$$

For simplicity, we introduce a uniform grid $x_\alpha := \alpha\Delta x$, where Δx is a small spatial scale and the corresponding finite volume cells $C_j := [x_{j-\frac{1}{2}}, x_{j+\frac{1}{2}}]$, and assume that at certain time level t, the solution is realized in terms of its cell averages, $\overline{\boldsymbol{U}}_j(t) = \frac{1}{\Delta x}\int_{C_j} \boldsymbol{U}(x,t)\,dx$, which are evolved in time according to the semi-discrete central-upwind scheme [8, 9, 27]:

$$\frac{d}{dt}\overline{\boldsymbol{U}}_j(t) = -\frac{\boldsymbol{H}_{j+\frac{1}{2}}(t) - \boldsymbol{H}_{j-\frac{1}{2}}(t)}{\Delta x} + \overline{\boldsymbol{S}}_j(t) + \overline{\boldsymbol{M}}_j(t) \tag{3.3}$$

with the central-upwind numerical fluxes, $\boldsymbol{H}_{j\pm\frac{1}{2}}$, given by

$$\boldsymbol{H}_{j+\frac{1}{2}} = \frac{a^+_{j+\frac{1}{2}}\boldsymbol{F}(\boldsymbol{U}^-_{j+\frac{1}{2}}, B_{j+\frac{1}{2}}) - a^-_{j+\frac{1}{2}}\boldsymbol{F}(\boldsymbol{U}^+_{j+\frac{1}{2}}, B_{j+\frac{1}{2}})}{a^+_{j+\frac{1}{2}} - a^-_{j+\frac{1}{2}}} + \frac{a^+_{j+\frac{1}{2}}a^-_{j+\frac{1}{2}}}{a^+_{j+\frac{1}{2}} - a^-_{j+\frac{1}{2}}}\left[\boldsymbol{U}^+_{j+\frac{1}{2}} - \boldsymbol{U}^-_{j+\frac{1}{2}}\right]. \tag{3.4}$$

Note that all of the indexed quantities in (3.4) depend on time, but from now on, we suppress the time-dependence of indexed quantities in order to shorten the notation.

In (3.4), $\boldsymbol{U}^\pm_{j+\frac{1}{2}}$ are the right and left point values of the piecewise linear reconstruction

$$\widetilde{\boldsymbol{U}}_j(x) = \overline{\boldsymbol{U}}_j + (\boldsymbol{U}_x)_j(x - x_j), \quad \forall x \in C_j, \ \forall j, \tag{3.5}$$

at $x = x_{j+\frac{1}{2}}$:

$$\boldsymbol{U}^+_{j+\frac{1}{2}} := \overline{\boldsymbol{U}}_{j+1} - \frac{\Delta x}{2}(\boldsymbol{U}_x)_{j+1}, \quad \boldsymbol{U}^-_{j+\frac{1}{2}} := \overline{\boldsymbol{U}}_j + \frac{\Delta x}{2}(\boldsymbol{U}_x)_j. \tag{3.6}$$

To ensure the second-order accuracy and a non-oscillatory nature of the reconstruction, the numerical derivatives $(\boldsymbol{U}_x)_j$ are to be computed using a nonlinear limiter, for example, the generalized minmod limiters:

$$(\boldsymbol{U}_x)_j = \text{minmod}\left(\theta\,\frac{\overline{\boldsymbol{U}}_{j+1} - \overline{\boldsymbol{U}}_j}{\Delta x}, \ \frac{\overline{\boldsymbol{U}}_{j+1} - \overline{\boldsymbol{U}}_{j-1}}{2\Delta x}, \ \theta\,\frac{\overline{\boldsymbol{U}}_j - \overline{\boldsymbol{U}}_{j-1}}{\Delta x}\right),$$

where the minmod function is defined by

DOI: 10.1002/fld

$$\text{minmod}(z_1,z_2,\ldots):=\begin{cases}\min(z_1,z_2,\ldots), & \text{if } z_i>0 \ \forall i,\\ \max(z_1,z_2,\ldots), & \text{if } z_i<0 \ \forall i,\\ 0, & \text{otherwise,}\end{cases}$$

and the parameter $\theta \in [1,2]$ controls the amount of numerical dissipation: The larger the θ, the smaller the numerical dissipation.

The use of a limiter does not, however, guarantee the positivity of $h^{\pm}_{j+\frac{1}{2}} := w^{\pm}_{j+\frac{1}{2}} - B_{j+\frac{1}{2}}$, where

$$B_{j+\frac{1}{2}} := \frac{B\left(x_{j+\frac{1}{2}}+0\right)+B\left(x_{j+\frac{1}{2}}-0\right)}{2}. \tag{3.7}$$

Hence, to ensure the positivity of $h^{\pm}_{j+\frac{1}{2}}$, we first replace the bottom topography function $B(x)$ with its continuous piecewise linear approximation,

$$\widetilde{B}(x) = B_{j-\frac{1}{2}} + (B_{j+\frac{1}{2}} - B_{j-\frac{1}{2}})\cdot\frac{x-x_{j-\frac{1}{2}}}{\Delta x}, \quad \forall x\in C_j, \ \forall j, \tag{3.8}$$

for which the following property is satisfied:

$$B_j := \widetilde{B}(x_j) = \frac{1}{\Delta x}\int\limits_{C_j}\widetilde{B}(x)\,dx = \frac{B_{j+\frac{1}{2}}+B_{j-\frac{1}{2}}}{2}. \tag{3.9}$$

Remark 3.1
Notice that for the slanted bottom topography ($B_x \equiv$ constant), $\widetilde{B}(x) \equiv B(x)$. Also notice that Equation (3.7) reduces to $B_{j+\frac{1}{2}} = B(x_{j+\frac{1}{2}})$ if B is continuous at $x = x_{j+\frac{1}{2}}$.

Next, the reconstruction for w near (almost) dry areas has to be corrected because the use of (3.6) may lead to negative values of $h^{\pm}_{j+\frac{1}{2}}$ as it was shown in [9]. We therefore propose the following correction procedure: In the cells, where the original reconstruction (3.6) produces negative values of h, we make the slope of h to be equal to the slope of B. Namely, we proceed as follows:

$$\begin{aligned}&\text{if } w^{-}_{j+\frac{1}{2}} < B_{j+\frac{1}{2}} \text{ or } w^{+}_{j-\frac{1}{2}} < B_{j-\frac{1}{2}}, \text{ then take } (w_x)_j = (B_x)_j\\ &\Longrightarrow \quad w^{-}_{j+\frac{1}{2}} = \overline{h}_j + B_{j+\frac{1}{2}}, \quad w^{+}_{j-\frac{1}{2}} = \overline{h}_j + B_{j-\frac{1}{2}},\end{aligned}$$

where $\overline{h}_j := \overline{w}_j - B_j$. This correction (unlike the correction procedure in [9] or its more sophisticated modification recently proposed in [3]) not only will guarantee the positivity of $h^{\pm}_{j+\frac{1}{2}}$ but also will be able to exactly reconstruct the steady-state solution (2.5).

It should also be pointed out that when the solution is expected to have (almost) dry areas, say, when the computational domain contains 'islands' and/or 'coastal areas', the values of h could be very small or even zero. This may not allow us to (accurately) compute the values of the velocity u, which may become artificially large. In such cases, when in some cells, the point values $h^{\pm}_{j\pm\frac{1}{2}}$ are smaller than an *a priori* chosen positive number ε, that is, $h^{\pm}_{j\pm\frac{1}{2}} < \varepsilon$, the piecewise linear reconstruction of q in (3.5) should be replaced with a piecewise linear reconstruction of u in the entire computational domain. Namely, the velocity at the cell centers is first computed by the desingularization formula

$$u_j = \frac{2\,\overline{h}_j\cdot\overline{q}_j}{\overline{h}_j^2+\max\left(\overline{h}_j^2,\varepsilon^2\right)}, \tag{3.10}$$

and then the point values of the velocity at the cell interfaces $x = x_{j+\frac{1}{2}}$ are obtained from

$$u^{+}_{j+\frac{1}{2}} := u_{j+1} - \frac{\Delta x}{2}(u_x)_{j+1}, \quad u^{-}_{j+\frac{1}{2}} := u_j + \frac{\Delta x}{2}(u_x)_j,$$

DOI: 10.1002/fld

where the numerical derivative $(u_x)_j$ are evaluated using the same nonlinear limiter as in (3.5). For consistency, the values of the discharge at cell interfaces are recomputed using $q^{\pm}_{j\pm\frac{1}{2}} = h^{\pm}_{j\pm\frac{1}{2}} \cdot u^{\pm}_{j\pm\frac{1}{2}}$.

Remark 3.2
We note that one may use other strategies to compute the desingularized velocity:

$$u = \frac{\sqrt{2}hq}{\sqrt{h^4 + \max(h^4, \varepsilon^4)}},$$

or

$$u = \begin{cases} \dfrac{q}{h}, & \text{if} \quad h > \varepsilon, \\ 0, & \text{otherwise}, \end{cases}$$

see, for example, the discussion in [9]. Our numerical experiments demonstrate that the proposed method is not sensitive to the selection of the desingularization procedure used.

Next, equipped with the values of $h^{\pm}_{j+\frac{1}{2}}$ and $u^{\pm}_{j+\frac{1}{2}}$, we complete the construction of the central-upwind flux (3.4) by estimating the one-sided local speeds of propagation as follows:

$$\begin{aligned} a^{+}_{j+\frac{1}{2}} &= \max\left\{u^{+}_{j+\frac{1}{2}} + \sqrt{gh^{+}_{j+\frac{1}{2}}},\, u^{-}_{j+\frac{1}{2}} + \sqrt{gh^{-}_{j+\frac{1}{2}}},\, 0\right\}, \\ a^{-}_{j+\frac{1}{2}} &= \min\left\{u^{+}_{j+\frac{1}{2}} - \sqrt{gh^{+}_{j+\frac{1}{2}}},\, u^{-}_{j+\frac{1}{2}} - \sqrt{gh^{-}_{j+\frac{1}{2}}},\, 0\right\}. \end{aligned} \tag{3.11}$$

The final step in the derivation of the semi-discrete scheme is the discretization of the source terms:

$$\overline{\boldsymbol{S}}_j(t) \approx \frac{1}{\Delta x}\int\limits_{C_j} \boldsymbol{S}(\boldsymbol{U}, R, B)\,dx, \quad \overline{\boldsymbol{M}}_j(t) \approx \frac{1}{\Delta x}\int\limits_{C_j} \boldsymbol{M}(\boldsymbol{U}, B)\,dx.$$

We calculate the first component of $\overline{\boldsymbol{S}}_j$ using the midpoint rule:

$$\overline{S}^{(1)}_j = R(x_j, t),$$

while approximate the geometric source in $\overline{S}^{(2)}_j$ using a special quadrature derived in [8, 9], which guarantees the well-balancedness of the resulting scheme:

$$\overline{S}^{(2)}_j = -g\overline{h}_j \frac{B_{j+\frac{1}{2}} - B_{j-\frac{1}{2}}}{\Delta x}. \tag{3.12}$$

The second component of $\overline{\boldsymbol{M}}_j$ is computed using the desingularization procedure (3.10):

$$\overline{M}^{(2)}_j = -g\,n^2 \left(\frac{2\,\overline{h}_j}{\overline{h}^2_j + \max\left(\overline{h}^2_j, \varepsilon^2\right)}\right)^{7/3} |q_j| q_j. \tag{3.13}$$

We remark that the semi-discrete scheme (3.3), (3.4) is a system of time-dependent ODEs, which should be solved using a high-order (at least second order accurate) and efficient method as we discuss in Section 3.3 in the succeeding texts.

DOI: 10.1002/fld

3.2. Two-dimensional central-upwind scheme

In this section, we describe the central-upwind scheme for the 2-D shallow water system (1.2). As in the 1-D case, we rewrite the system (1.2) in terms of the new unknown vector $\boldsymbol{U} = (w, q := hu, p := hv)^T$:

$$\boldsymbol{U}_t + \boldsymbol{F}(\boldsymbol{U}, B)_x + \boldsymbol{G}(\boldsymbol{U}, B)_y = \boldsymbol{S}(\boldsymbol{U}, R, B) + \boldsymbol{M}(\boldsymbol{U}, B), \tag{3.14}$$

where the fluxes and the source terms are:

$$\begin{aligned}
\boldsymbol{F}(\boldsymbol{U}, B) &= \left(q, \frac{q^2}{w-B} + \frac{g}{2}(w-B)^2, \frac{qp}{w-B}\right)^T,\\
\boldsymbol{G}(\boldsymbol{U}, B) &= \left(p, \frac{qp}{w-B}, \frac{p^2}{w-B} + \frac{g}{2}(w-B)^2\right)^T,\\
\boldsymbol{S}(\boldsymbol{U}, R, B) &= \left(R, -g(w-B)B_x, -g(w-B)B_y\right),\\
\boldsymbol{M}(\boldsymbol{U}, B) &= \left(0, -g\frac{n^2}{h^{7/3}}q\sqrt{q^2+p^2}, -g\frac{n^2}{h^{7/3}}p\sqrt{q^2+p^2}\right)^T.
\end{aligned}$$

We denote by $C_{j,k}$ the computational cells $C_{j,k} = [x_{j-\frac{1}{2}}, x_{j+\frac{1}{2}}] \times [y_{k-\frac{1}{2}}, y_{k+\frac{1}{2}}]$, where $x_\alpha := \alpha\Delta x$ and $y_\beta := \beta\Delta y$, where Δx and Δy are small spatial scales, and write a central-upwind semi-discretization of (3.14) as the system of ODEs:

$$\frac{d}{dt}\overline{\boldsymbol{U}}_{j,k} = -\frac{\boldsymbol{H}^x_{j+\frac{1}{2},k} - \boldsymbol{H}^x_{j-\frac{1}{2},k}}{\Delta x} - \frac{\boldsymbol{H}^y_{j,k+\frac{1}{2}} - \boldsymbol{H}^y_{j,k-\frac{1}{2}}}{\Delta y} + \overline{\boldsymbol{S}}_{j,k} + \overline{\boldsymbol{M}}_{j,k}, \tag{3.15}$$

for the time evolution of the cell averages, $\overline{\boldsymbol{U}}_{j,k}(t) = \frac{1}{\Delta x\Delta y}\iint_{C_{j,k}} \boldsymbol{U}(x, y, t)\, dxdy$. As in the 1-D case, we follow [9, 29] and obtain the central-upwind numerical fluxes in the form

$$\begin{aligned}
\boldsymbol{H}^x_{j+\frac{1}{2},k} =& \frac{a^+_{j+\frac{1}{2},k}\boldsymbol{F}\left(\boldsymbol{U}^E_{j,k}, B_{j+\frac{1}{2},k}\right) - a^-_{j+\frac{1}{2},k}\boldsymbol{F}\left(\boldsymbol{U}^W_{j+1,k}, B_{j+\frac{1}{2},k}\right)}{a^+_{j+\frac{1}{2},k} - a^-_{j+\frac{1}{2},k}}\\
&+ \frac{a^+_{j+\frac{1}{2},k}a^-_{j+\frac{1}{2},k}}{a^+_{j+\frac{1}{2},k} - a^-_{j+\frac{1}{2},k}}\left[\boldsymbol{U}^W_{j+1,k} - \boldsymbol{U}^E_{j,k}\right],\\
\boldsymbol{H}^y_{j,k+\frac{1}{2}} =& \frac{b^+_{j,k+\frac{1}{2}}\boldsymbol{G}\left(\boldsymbol{U}^N_{j,k}, B_{j,k+\frac{1}{2}}\right) - b^-_{j,k+\frac{1}{2}}\boldsymbol{G}\left(\boldsymbol{U}^S_{j,k+1}, B_{j,k+\frac{1}{2}}\right)}{b^+_{j,k+\frac{1}{2}} - b^-_{j,k+\frac{1}{2}}}\\
&+ \frac{b^+_{j,k+\frac{1}{2}}b^-_{j,k+\frac{1}{2}}}{b^+_{j,k+\frac{1}{2}} - b^-_{j,k+\frac{1}{2}}}\left[\boldsymbol{U}^S_{j,k+1} - \boldsymbol{U}^N_{j,k}\right].
\end{aligned} \tag{3.16}$$

Here, $B_{j\pm\frac{1}{2},k}$ and $B_{j,k\pm\frac{1}{2}}$ are the values of the piecewise bilinear approximation of B:

$$\begin{aligned}
\widetilde{B}(x, y) =& B_{j-\frac{1}{2},k-\frac{1}{2}} + \left(B_{j+\frac{1}{2},k-\frac{1}{2}} - B_{j-\frac{1}{2},k-\frac{1}{2}}\right)\cdot\frac{x - x_{j-\frac{1}{2}}}{\Delta x}\\
&+ \left(B_{j-\frac{1}{2},k+\frac{1}{2}} - B_{j-\frac{1}{2},k-\frac{1}{2}}\right)\cdot\frac{y - y_{k-\frac{1}{2}}}{\Delta y} + \left(B_{j+\frac{1}{2},k+\frac{1}{2}} - B_{j+\frac{1}{2},k-\frac{1}{2}}\right.\\
&\left.- B_{j-\frac{1}{2},k+\frac{1}{2}} + B_{j-\frac{1}{2},k-\frac{1}{2}}\right)\frac{\left(x - x_{j-\frac{1}{2}}\right)\left(y - y_{k-\frac{1}{2}}\right)}{\Delta x\Delta y}, \quad (x, y) \in C_{j,k},
\end{aligned} \tag{3.17}$$

DOI: 10.1002/fld

with $B_{j+\frac{1}{2},k+\frac{1}{2}} = B\left(x_{j+\frac{1}{2}}, y_{k+\frac{1}{2}}\right)$ if the function B is continuous at $\left(x_{j+\frac{1}{2}}, y_{k+\frac{1}{2}}\right)$; see [9] for the case of discontinuous B.

Similarly to the 1-D case, the piecewise bilinear approximant $\widetilde{B}$ satisfies the following property:

$$B_{j,k} := \widetilde{B}(x_j, y_k) = \frac{1}{\Delta x \Delta y} \iint\limits_{C_{j,k}} \widetilde{B}(x,y)\,dx\,dy = \frac{1}{4}\left(B_{j+\frac{1}{2},k} + B_{j-\frac{1}{2},k} + B_{j,k+\frac{1}{2}} + B_{j,k-\frac{1}{2}}\right), \tag{3.18}$$

where $B_{j+\frac{1}{2},k} := \widetilde{B}\left(x_{j+\frac{1}{2}}, y_k\right)$ and $B_{j,k+\frac{1}{2}} := \widetilde{B}\left(x_j, y_{k+\frac{1}{2}}\right)$.

Remark 3.3
For the slanted bottom topography satisfying either $B_x \equiv$ constant, $B_y \equiv 0$ or $B_x \equiv 0$, $B_y \equiv$ constant, the approximant (3.17) is exact, that is, $\widetilde{B}(x,y) \equiv B(x,y)$.

The values $\boldsymbol{U}^{E,W,N,S}_{j,k}$ in (3.16) are the point values of the piecewise linear reconstruction

$$\widetilde{\boldsymbol{U}}(x,y) = \overline{\boldsymbol{U}}_{j,k} + (\boldsymbol{U}_x)_{j,k}(x - x_j) + (\boldsymbol{U}_y)_{j,k}(y - y_k), \quad (x,y) \in C_{j,k}, \tag{3.19}$$

at $(x_{j+\frac{1}{2}}, y_k)$, $(x_{j-\frac{1}{2}}, y_k)$, $(x_j, y_{k+\frac{1}{2}})$, $(x_j, y_{k-\frac{1}{2}})$, respectively. Namely, we have

$$\begin{aligned}
\boldsymbol{U}^E_{j,k} &:= \widetilde{\boldsymbol{U}}\left(x_{j+\frac{1}{2}} - 0, y_k\right) = \overline{\boldsymbol{U}}_{j,k} + \frac{\Delta x}{2}(\boldsymbol{U}_x)_{j,k}\,,\\
\boldsymbol{U}^W_{j,k} &:= \widetilde{\boldsymbol{U}}\left(x_{j-\frac{1}{2}} + 0, y_k\right) = \overline{\boldsymbol{U}}_{j,k} - \frac{\Delta x}{2}(\boldsymbol{U}_x)_{j,k}\,,\\
\boldsymbol{U}^N_{j,k} &:= \widetilde{\boldsymbol{U}}\left(x_j, y_{k+\frac{1}{2}} - 0\right) = \overline{\boldsymbol{U}}_{j,k} + \frac{\Delta y}{2}(\boldsymbol{U}_y)_{j,k}\,,\\
\boldsymbol{U}^S_{j,k} &:= \widetilde{\boldsymbol{U}}\left(x_j, y_{k-\frac{1}{2}} + 0\right) = \overline{\boldsymbol{U}}_{j,k} - \frac{\Delta y}{2}(\boldsymbol{U}_y)_{j,k}\,.
\end{aligned}$$

As in the 1-D case, the numerical derivatives $(\boldsymbol{U}_x)_{j,k}$ and $(\boldsymbol{U}_y)_{j,k}$ are to be computed using a nonlinear limiter, say, the generalized minmod limiter (for details, see [9]).

To preserve the positivity of water height h, we follow the 1-D approach presented in Section 3.1 and correct the reconstructed values of w as follows:

$$\begin{aligned}
&\text{if } w^E_{j,k} < B_{j+\frac{1}{2},k} \text{ or } w^W_{j,k} < B_{j-\frac{1}{2},k}, \text{ then take } (w_x)_{j,k} = (B_x)_{j,k}\\
&\Longrightarrow w^E_{j,k} = B_{j+\frac{1}{2},k} + \overline{h}_{j,k}, \quad w^W_{j,k} = B_{j-\frac{1}{2},k} + \overline{h}_{j,k};\\
&\text{if } w^N_{j,k} < B_{j,k+\frac{1}{2}} \text{ or } w^S_{j,k} < B_{j,k-\frac{1}{2}}, \text{ then take } (w_y)_{j,k} = (B_y)_{j,k}\\
&\Longrightarrow w^N_{j,k} = B_{j,k+\frac{1}{2}} + \overline{h}_{j,k}, \quad w^S_{j,k} = B_{j,k-\frac{1}{2}} + \overline{h}_{j,k},
\end{aligned}$$

where $\overline{h}_{j,k} := \overline{w}_{j,k} - B_{j,k}$.

Once again, we observe that the obtained point values of h may be very small or even zero. Similarly, to the 1-D case, when the solution contains (almost) dry areas, that is, if $h_{j+\frac{1}{2},k} < \varepsilon$ or $h_{j,k+\frac{1}{2}} < \varepsilon$ somewhere in the computational domain, we reconstruct the velocities u and v instead of the discharges q and p. To this end, we first compute the velocities at the cell centers:

$$u_{j,k} = \frac{2\,\overline{h}_{j,k}\,\overline{q}_{j,k}}{\overline{h}^2_{j,k} + \max\left(\overline{h}^2_{j,k}, \varepsilon^2\right)}, \quad v_{j,k} = \frac{2\,\overline{h}_{j,k}\,\overline{p}_{j,k}}{\overline{h}^2_{j,k} + \max\left(\overline{h}^2_{j,k}, \varepsilon^2\right)}, \tag{3.20}$$

DOI: 10.1002/fld

and evaluate the point values at the cell interfaces using the piecewise linear reconstructions:

$$
\begin{aligned}
u^{\mathrm{E}}_{j,k} &:= u_{j,k} + \frac{\Delta x}{2}(u_x)_{j,k}, \quad u^{\mathrm{W}}_{j,k} := u_{j,k} - \frac{\Delta x}{2}(u_x)_{j,k},\\
u^{\mathrm{N}}_{j,k} &:= u_{j,k} + \frac{\Delta y}{2}(u_y)_{j,k}, \quad u^{\mathrm{S}}_{j,k} := u_{j,k} - \frac{\Delta y}{2}(u_y)_{j,k}\\
v^{\mathrm{E}}_{j,k} &:= v_{j,k} + \frac{\Delta x}{2}(v_x)_{j,k}, \quad v^{\mathrm{W}}_{j,k} : v_{j,k} - \frac{\Delta x}{2}(v_x)_{j,k},\\
v^{\mathrm{N}}_{j,k} &:= v_{j,k} + \frac{\Delta y}{2}(v_y)_{j,k}, \quad v^{\mathrm{S}}_{j,k} := v_{j,k} - \frac{\Delta y}{2}(v_y)_{j,k},
\end{aligned}
$$

where the numerical derivatives $(u_x)_{j,k}, (v_x)_{j,k}, (u_y)_{j,k}$, and $(v_y)_{j,k}$ are computed with the help of the same nonlinear limiter used in (3.19). The obtained values are then used to recompute the corresponding point values of q and p:

$$
q^{\mathrm{E(W,N,S)}}_{j,k} = h^{\mathrm{E(W,N,S)}}_{j,k} \cdot u^{\mathrm{E(W,N,S)}}_{j,k}, \qquad p^{\mathrm{E(W,N,S)}}_{j,k} = h^{\mathrm{E(W,N,S)}}_{j,k} \cdot v^{\mathrm{E(W,N,S)}}_{j,k}.
$$

The local one-sided speeds of propagation $a^{\pm}_{j+\frac{1}{2},k}$ and $b^{\pm}_{j,k+\frac{1}{2}}$ in (3.16) can be estimated as follows:

$$
\begin{aligned}
a^{+}_{j+\frac{1}{2},k} &= \max\{u^{E}_{j,k} + \sqrt{gh^{E}_{j,k}},\, u^{W}_{j+1,k} + \sqrt{gh^{W}_{j+1,k}},\, 0\},\\
a^{-}_{j+\frac{1}{2},k} &= \min\{u^{E}_{j,k} - \sqrt{gh^{E}_{j,k}},\, u^{W}_{j+1,k} - \sqrt{gh^{W}_{j+1,k}},\, 0\},\\
b^{+}_{j,k+\frac{1}{2}} &= \max\{v^{N}_{j,k} + \sqrt{gh^{N}_{j.k}},\, v^{S}_{j,k+1} + \sqrt{gh^{S}_{j,k+1}},\, 0\},\\
b^{-}_{j,k+\frac{1}{2}} &= \min\{v^{N}_{j,k} - \sqrt{gh^{N}_{j.k}},\, v^{S}_{j,k+1} - \sqrt{gh^{S}_{j,k+1}},\, 0\}.
\end{aligned}
\tag{3.21}
$$

Finally, a well-balanced discretization of the source term is obtained using the same desingularization process as in (3.20) and is thus given by

$$
\begin{aligned}
&S^{(1)}_{j,k} = R(x_j, y_k, t), && M^{(1)}_{j,k} = 0,\\
&S^{(2)}_{j,k} = -g\overline{h}_{j,k}\frac{B_{j+\frac{1}{2},k} - B_{j-\frac{1}{2},k}}{\Delta x}, && M^{(2)}_{j,k} = -gn^2\sqrt{\overline{q}^2_{j,k} + \overline{p}^2_{j,k}}\left(\frac{2\overline{h}_{j,k}}{\overline{h}^2_{j,k} + \max\left(\overline{h}^2_{j,k}, \varepsilon^2\right)}\right)^{7/3} q_{j,k},\\
&S^{(3)}_{j,k} = -g\overline{h}_{j,k}\frac{B_{j,k+\frac{1}{2}} - B_{j,k-\frac{1}{2}}}{\Delta y}, && M^{(3)}_{j,k} = -gn^2\sqrt{\overline{q}^2_{j,k} + \overline{p}^2_{j,k}}\left(\frac{2\overline{h}_{j,k}}{\overline{h}^2_{j,k} + \max\left(\overline{h}^2_{j,k}, \varepsilon^2\right)}\right)^{7/3} p_{j,k}.
\end{aligned}
$$

As in the 1-D case, in order to obtain a fully discrete scheme, the system (3.15), (3.16) should be integrated by a stable and efficient ODE solver of at least second order of accuracy. We discuss the details of time integration in the next section.

3.3. Time integration method

As it was outlined in the previous sections, both the 1-D and 2-D semi-discrete central-upwind schemes are the systems of time-dependent ODEs that should be solved by an accurate, stable, and efficient method. A family of explicit strong stability preserving Runge-Kutta methods (SSP-RK) has been widely used in numerical simulations of various shallow water systems, see, for example, [33, 34]. The presence of the stiff friction term in both (3.3) and (3.15) can lead, however, to a great loss in accuracy and efficiency of the ODE solver. In shallow water applications that included dry and/or almost dry areas, the explicit treatment of the friction terms imposes a severe time step restriction, which is several order of magnitude smaller than a typical time step used for the corresponding friction-free version of the studied system.

DOI: 10.1002/fld

An attractive alternative to explicit methods is implicit-explicit SSP Runge-Kutta solvers, which treat the stiff part of the underlying ODE system implicitly and thus typically have the stability domains based on the nonstiff term only, see, for example, [35–40]. However, a straightforward implementation of these methods may break the discrete balance between the fluxes, geometric source, and the friction terms maintained by the derived semi-discrete central-upwind scheme, and the resulting fully discrete method will not be able to preserve the relevant steady states and the positivity of the computed water depth.

To overcome this difficulty, we have recently developed a family of second-order semi-implicit time integration methods for systems of ODEs with stiff damping term [31]. In these methods, only a portion of the stiff term is implicitly treated, and therefore, the evolution equation is very easy to solve and implement compared to fully implicit or implicit-explicit methods. The important feature of the ODE solvers we introduced in [31] resides in the fact that they are capable of exactly preserving the steady states as well as maintaining the sign of the computed solution under the time step restriction determined by the nonstiff part of the system only. The new semi-implicit methods are based on the modification of explicit SSP-RK methods and are proven to have a formal second order of accuracy, $A(\alpha)$-stability and stiff decay. We now briefly describe the application of the second-order semi-implicit ODE solver from [31] to the ODE system (3.3), (3.4) (the implementation of the ODE solver to the system (3.15), (3.16) is similar, and we thus omit it for the sake of brevity).

We first introduce the grid function of the numerical solution $\overline{\boldsymbol{U}} := \left\{\overline{\boldsymbol{U}}_j\right\}$. We then denote the discretization of the sum of fluxes, geometric, and water source terms by

$$\boldsymbol{\mathcal{F}}\left[\overline{\boldsymbol{U}}\right]_j := -\frac{\boldsymbol{H}_{j+\frac{1}{2}} - \boldsymbol{H}_{j-\frac{1}{2}}}{\Delta x} + \boldsymbol{S}_j, \tag{3.22}$$

and introduce the discrete friction coefficient

$$\mathcal{G}(\overline{\boldsymbol{U}}_j) := -gn^2\left(\frac{2\,\overline{h}_j}{\overline{h}_j^2 + \max\left(\overline{h}_j^2, \varepsilon^2\right)}\right)^{7/3}|\overline{q}_j|, \tag{3.23}$$

so that the discretization of the friction term (3.13) can be written as $\overline{M}_j^{(2)} = \mathcal{G}(\overline{\boldsymbol{U}}_j)\,\overline{q}_j$. Using these notations, the ODE system (3.3) can be rewritten as

$$\begin{cases} \dfrac{d}{dt}\,\overline{w}_j = \mathcal{F}^{(1)}[\overline{\boldsymbol{U}}]_j, \\ \dfrac{d}{dt}\,\overline{q}_j = \mathcal{F}^{(2)}[\overline{\boldsymbol{U}}]_j + \mathcal{G}(\overline{\boldsymbol{U}}_j)\,\overline{q}_j. \end{cases} \tag{3.24}$$

We now implement the SI-RK3 method to the system (3.24) (the SI-RK3 method is a second-order semi-implicit Runge-Kutta method based on the third-order SSP-RK method; for details, see [31, Section 3]). The resulting fully discrete scheme can be written as

$$\begin{aligned} w_j^I &= \overline{w}_j(t) + \Delta t\,\mathcal{F}^{(1)}[\overline{\boldsymbol{U}}(t)]_j, \\ q_j^I &= \frac{\overline{q}_j(t) + \Delta t\,\mathcal{F}^{(2)}[\overline{\boldsymbol{U}}(t)]_j}{1 - \Delta t\,\mathcal{G}(\overline{\boldsymbol{U}}(t)_j)}, \end{aligned} \tag{3.25a}$$

$$\begin{aligned} \overline{w}_j^{II} &= \frac{3}{4}\,\overline{w}_j(t) + \frac{1}{4}\left(\overline{w}_j^I + \Delta t\,\mathcal{F}^{(1)}[\overline{\boldsymbol{U}}^I]_j\right), \\ \overline{q}_j^{II} &= \frac{3}{4}\,\overline{q}_j(t) + \frac{1}{4}\cdot\frac{\overline{q}_j^I + \Delta t\,\mathcal{F}^{(2)}[\overline{\boldsymbol{U}}^I]_j}{1 - \Delta t\,\mathcal{G}(\overline{\boldsymbol{U}}_j^I)}, \end{aligned} \tag{3.25b}$$

DOI: 10.1002/fld

$$\begin{aligned}\overline{w}_j^{III} &= \frac{1}{3}\,\overline{w}_j(t) + \frac{2}{3}\left(\overline{w}_j^{II} + \Delta t\,\mathcal{F}^{(1)}[\overline{\boldsymbol{U}}^{II}]_j\right),\\ \overline{q}_j^{III} &= \frac{1}{3}\,\overline{q}_j(t) + \frac{2}{3}\cdot\frac{\overline{q}_j^{II} + \Delta t\,\mathcal{F}^{(2)}[\overline{\boldsymbol{U}}^{II}]_j}{1-\Delta t\,\mathcal{G}(\overline{\boldsymbol{U}}_j^{II})},\end{aligned} \tag{3.25c}$$

$$\begin{aligned}\overline{w}_j(t+\Delta t) &= \overline{w}_j^{III},\\ \overline{q}_j(t+\Delta t) &= \frac{\overline{q}_j^{III} - (\Delta t)^2\mathcal{F}^{(2)}[\overline{\boldsymbol{U}}^{III}]_j\,\mathcal{G}(\overline{\boldsymbol{U}}_j^{III})}{1+(\Delta t\,\mathcal{G}(\overline{\boldsymbol{U}}_j^{III}))^2},\end{aligned} \tag{3.25d}$$

where $\overline{\boldsymbol{U}}^{I} = (w^{I}, q^{I})^T$, $\overline{\boldsymbol{U}}^{II} = (w^{II}, q^{II})^T$, and $\overline{\boldsymbol{U}}^{III} = (w^{III}, q^{III})^T$.

In the following theorem, we prove that the fully discrete scheme (3.25) is well-balanced.

Theorem 3.1

The fully discrete central-upwind scheme (3.25) is well-balanced in the sense that it preserves steady-state solutions satisfying

$$h \equiv h_0 = \left(\frac{n^2q_0^2}{C}\right)^{3/10}, \quad q \equiv q_0, \quad B_x \equiv -C, \quad R \equiv 0 \tag{3.26}$$

as long as $h_0 \geqslant \varepsilon$, where ε is a desingularization parameter used in (3.10).

Proof

We first note that for the steady states (3.26), the numerical derivatives of $\boldsymbol{U}$ are given by $\boldsymbol{U}_x \equiv (-C, 0)^T$, and the numerical flux reduces to

$$\boldsymbol{H}_{j+\frac{1}{2}} = \left(q_0, \frac{q_0^2}{h_0} + \frac{g}{2}h_0^2\right)^T.$$

Therefore, $\boldsymbol{H}_{j+\frac{1}{2}} - \boldsymbol{H}_{j-\frac{1}{2}} \equiv \boldsymbol{0}$. The sums of the components of the source terms are also equal to zero, that is,

$$\overline{S}_j^{(1)} + \overline{M}_j^{(1)} = 0 + 0 = 0, \quad \overline{S}_j^{(2)} + \overline{M}_j^{(2)} = gh_0C - g\frac{n^2}{h_0^{7/3}}|q_0|q_0 = 0. \tag{3.27}$$

The second equation can be proven true when $h_0 \geqslant \varepsilon$ according to the definition of h_0. Then, using the notations (3.22) and (3.23), we obtain that (3.27) is equivalent to

$$\mathcal{F}^{(1)}[\overline{\boldsymbol{U}}]_j = 0, \quad \mathcal{F}^{(2)}[\overline{\boldsymbol{U}}]_j + \mathcal{G}(\overline{\boldsymbol{U}}_j)\,\overline{q}_j = 0,$$

which after being substituted into (3.25) implies $\overline{h}_j^{n+1} = \overline{h}_j^n = h_0$ and $\overline{q}_j^{n+1} = \overline{q}_j^n = q_0$. We therefore have proved that the steady state (3.26) is preserved. □

Remark 3.4

Notice that the 2-D version of Theorem 3.1 can be proved in a similar manner.

Remark 3.5

In [31], we have proved that the time step restriction for the SI-RK3 method is determined by the nonstiff (explicitly treated) term only and no extra time restrictions due to the stiffness of the friction term is required. This implies that for the ODE system (3.24), arising from the central-upwind semi-discretization of the 1-D shallow water system, the size of the time step is to be calculated based on the CFL condition, namely, we need to select

DOI: 10.1002/fld

$$\Delta t \leqslant (\Delta t)_* := \frac{\Delta x}{2a}, \quad a = \max_j \left\{ a^+_{j+\frac{1}{2}}, -a^-_{j+\frac{1}{2}} \right\}, \tag{3.28}$$

where $a^{\pm}_{j+\frac{1}{2}}$ are the local propagation speeds defined in (3.11).

Remark 3.6

We would like to emphasize that [9, Theorem 2.1] directly applies to the first stage of the SI-RK3 method (3.25), and hence, the time step restriction (3.28) guarantees the positivity of $\overline{h}^I_j := \overline{w}^I_j - B_j$ for all j provided $\overline{h}_j(t) \geqslant 0$ for all j. The positivity of $\overline{h}^{II}_j$, $\overline{h}^{III}_j$, and $\overline{h}_j(t+\Delta t)$ will then be ensured by the same theorem provided $\Delta t \leqslant (\Delta t)^I_*$ and $\Delta t \leqslant (\Delta t)^{II}_*$, where $(\Delta t)^I_*$ and $(\Delta t)^{II}_*$ are computed using (3.28) applied to the intermediate solutions $\overline{\boldsymbol{U}}^I$ and $\overline{\boldsymbol{U}}^{II}$, respectively. To satisfy all of the aforementioned time step restrictions, we implement the following adaptive strategy:

(i) Given the solution $\overline{\boldsymbol{U}}(t)$, set $\Delta t := \kappa(\Delta t)_*$, where $\kappa \in (0,1)$ and $(\Delta t)_*$ is given by (3.28);
(ii) Use Δt to compute $\overline{\boldsymbol{U}}^I$ by (3.25a);
(iii) Given the intermediate solution $\overline{\boldsymbol{U}}^I$, compute $(\Delta t)^I_*$ by (3.28);
(iv) If $(\Delta t)^I_* < \Delta t$, set $\Delta t := \kappa(\Delta t)^I_*$ and go back to Step (ii);
(v) Use Δt to compute $\overline{\boldsymbol{U}}^{II}$ by (3.25b);
(vi) Given the intermediate solution $\overline{\boldsymbol{U}}^{II}$, compute $(\Delta t)^{II}_*$ by (3.28);
(vii) If $(\Delta t)^{II}_* < \Delta t$, set $\Delta t := \kappa(\Delta t)^{II}_*$ and go back to Step (ii);
(viii) Use Δt to compute $\overline{\boldsymbol{U}}^{III}$ and $\overline{\boldsymbol{U}}(t+\Delta t)$ by (3.25c) and (3.25d), respectively.

In all of the numerical examples in the succeeding texts, we have used $\kappa = 0.9$.

In the 2-D case, we have implemented a similar adaptive strategy to ensure the positivity of h. However, the basic CFL condition is more restrictive (see [9, Theorem 3.1]), and one has to choose

$$\Delta t \leqslant (\Delta t)_* := \min\left\{ \frac{\Delta x}{4a}, \frac{\Delta y}{4b} \right\}, \ a = \max_{j,k} \left\{ a^+_{j+\frac{1}{2},k}, -a^-_{j+\frac{1}{2},k} \right\}, \ b = \max_{j,k} \left\{ b^+_{j,k+\frac{1}{2}}, -b^-_{j,k+\frac{1}{2}} \right\},$$

where $a^{\pm}_{j+\frac{1}{2},k}$ and $b^{\pm}_{j,k+\frac{1}{2}}$ are the local propagation speeds defined in (3.21).

4. NUMERICAL EXAMPLES

In this section, we test the designed well-balanced positivity preserving central-upwind scheme on several 1-D and 2-D problems including the ones with the data originating from the recently performed laboratory experiments reported in [32]. In all of the examples in the succeeding texts, the gravitation constant $g = 9.8$ (in Example 4, we use $g = 9.81$), the minmod parameter $\theta = 1.3$, and we select the desingularization parameter $\varepsilon = 10^{-8}$ (in Example 4, we use $\varepsilon = 10^{-4}$, 10^{-8}, and 10^{-12}).

4.1. One-dimensional examples

Example 1 – Steady flow over a slanted surface. We begin by illustrating the well-balanced property of the designed scheme, that is, we test the ability of the scheme to exactly preserve the steady-state solution (2.5), which is schematically shown in Figure 1 (left). To this end, we consider the system (2.1) on the interval $[0, 2.5]$ with $R \equiv 0$ and subject to the constant initial data given by (2.5). We introduce a uniform grid with $\Delta x = 0.025$ and set zero-order extrapolation boundary conditions at both ends of the domain, that is, $\overline{h}_0 = \overline{h}_1, \overline{h}_{N+1} = \overline{h}_N$. We run five sets of experiments with different values of h_0, q_0, B_x, and n, shown in Table I, in which the first four are taken from [32]. The solution is evolved until time $t = 100$. The right column of Table I clearly illustrates that our scheme preserves the studied steady-state solutions within machine accuracy.

DOI: 10.1002/fld

Example 2 – Small perturbation of steady flow over a slanted surface. In this example, we take the same initial data from Example 1 but introduce a small perturbation to the initial water surface, namely,

$$h(x,0) = h_0 + \begin{cases} 0.2h_0, & 1 \leqslant x \leqslant 1.25, \\ 0, & \text{otherwise}, \end{cases} \qquad q(x,0) \equiv q_0. \tag{4.1}$$

We first consider a supercritical case (Test 2 in Table I) and present several time snapshots of the computed solution in Figure 2. As one can see, the perturbation first changes its shape and propagates to the right, eventually leaving the domain. At large times, the computed solution converges to the steady state (Figure 2 (right)).

We then proceed with a subcritical case (Test 4 in Table I) and again replace the initial data in Example 1 with (4.1). The evolution of the perturbed solution is shown in Figure 3. In this case, the shape of the propagating perturbation is different from the one in the supercritical case, but at large times, the computed solution still converges to the steady state.

Finally, we consider Test 5 from Table I, in which the magnitude of the slope B_x is much larger than in the other tests. In this case, the perturbation propagates much faster than in the previous two tests (Figure 4), but the scheme still performs very well and the numerical steady state is achieved at large times.

Example 3 – Rainfall-runoff over a slanted surface. In this example, which is a 1-D modification of Example T3 from [24], we test the stability and accuracy of the proposed numerical scheme in

Table I. Example 1: Errors in computing the steady-state solution (2.5) for different sets of data.

Test	h_0	q_0	n	B_x	Froude number	$\|h-h_0\|_\infty$
1	0.57708	2	0.02	−0.01	1.46	3.3307×10^{-16}
2	0.09564	0.1	0.02	−0.01	1.08	5.8287×10^{-16}
3	0.25119	0.1	0.1	−0.01	0.25	1.0547×10^{-15}
4	0.02402	0.002	0.1	−0.01	0.17	1.8978×10^{-15}
5	0.44894	2	0.1	$-1/\sqrt{3}$	2.12	4.9960×10^{-16}

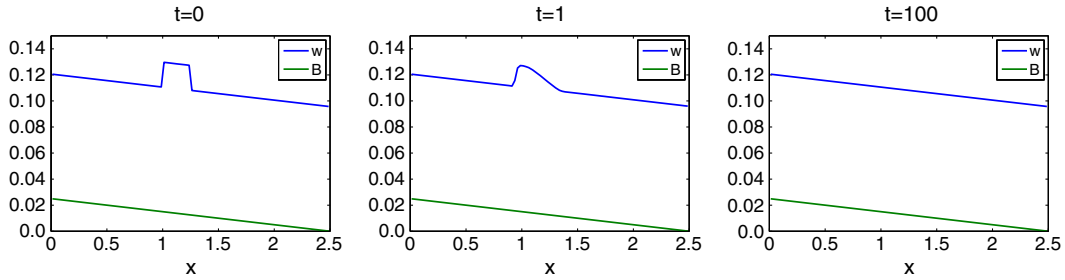

Figure 2. Example 2: Evolution of the solution in the supercritical case (Test 2 in Table I).

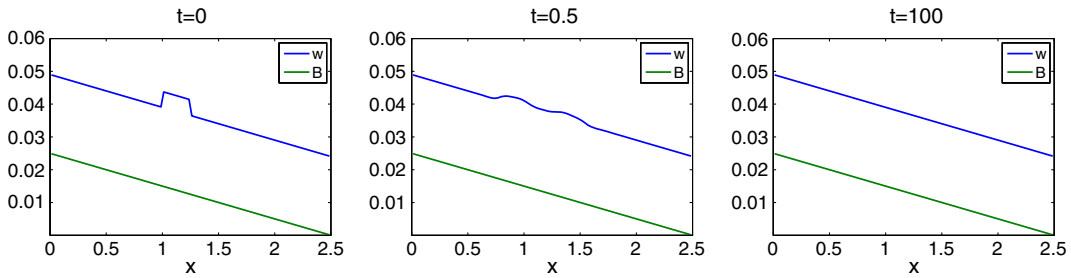

Figure 3. Example 2: Evolution of the solution in the subcritical case (Test 4 in Table I).

DOI: 10.1002/fld

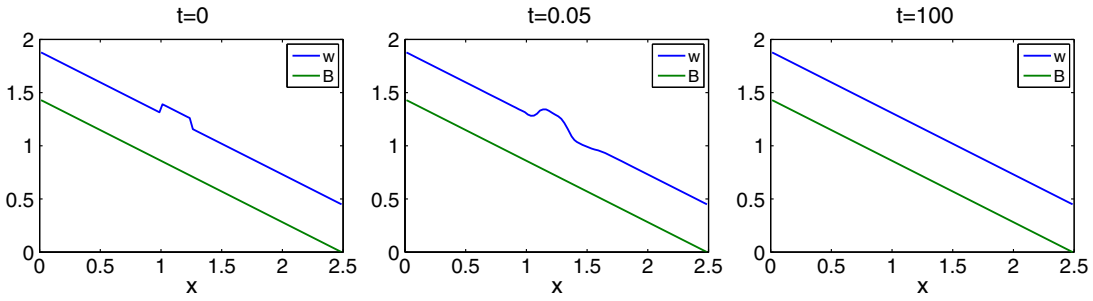

Figure 4. Example 2: Evolution of the solution with large bottom slope (Test 5 in Table I).

Table II. Example 3: Friction coefficients and slopes.

Test	1	2	3	4	5	6
n	0.02	0.05	0.02	0.05	0.02	0.05
B_x	−0.05	−0.05	−0.01	−0.01	−0.2	−0.2

the scenario with very shallow water, bed friction, and large bottom slope. The surface is assumed to be dry at time $t = 0$, that is, we set

$$h(x,0) \equiv 0, \quad q(x,0) \equiv 0, \tag{4.2}$$

and the bottom is set to be a slanted surface. The rain of a constant intensity starts falling at time $t = 0$ and stops at time $t = 100$. This is modeled by taking

$$R(x,t) = \begin{cases} 10^{-4}, & 0 \leqslant t \leqslant 100, \\ 0, & \text{otherwise.} \end{cases}$$

The water drains through the right boundary, at which we set

$$\overline{h}_{N+1} := 0, \quad \overline{q}_{N+1} := 0,$$

where N is a total number of cells inside the computational domain $[0, 2.5]$ (we take $N = 100$ in this example). On the left side of the domain, we use solid wall boundary conditions.

We consider six sets of data with different values of friction coefficient n and slope B_x (Table II) and run the simulations until time $t = 150$.

In Figure 5, we plot the first component of the numerical flux at the right edge of the computational domain ($H^{(1)}_{N+1/2}$) as a function of time. Notice that this is an approximation of the outlet discharge, which is a measurable quantity in experimental settings. In all six cases, the results obtained by the designed central-upwind scheme are in a good agreement with the results reported in [24]. We would like to point out that in [24], the simulations were performed in the 2-D domain of the width 0.2, so that all of the discharge values in Figure 5 are to be multiplied by the factor of 0.2 in order to be compared with those in [24]. As one can clearly see from Figure 5, the reported results are oscillation-free confirming the robustness of the designed central-upwind scheme.

Remark 4.1

It should be observed that if an upwind numerical scheme is used instead of the central-upwind one, the ghost cell values (4.2) may be unacceptable. We refer the reader to [24], where supercritical boundary conditions have been implemented using a different ghost cell values:

$$\overline{h}_{N+1} := \left(\frac{\overline{q}^2_N}{g}\right)^{1/3}, \quad \overline{q}_{N+1} := \overline{q}_N.$$

In all of our computations, both types of boundary conditions produce similar results. However, the supercritical boundary conditions sometime cause small oscillations.

DOI: 10.1002/fld

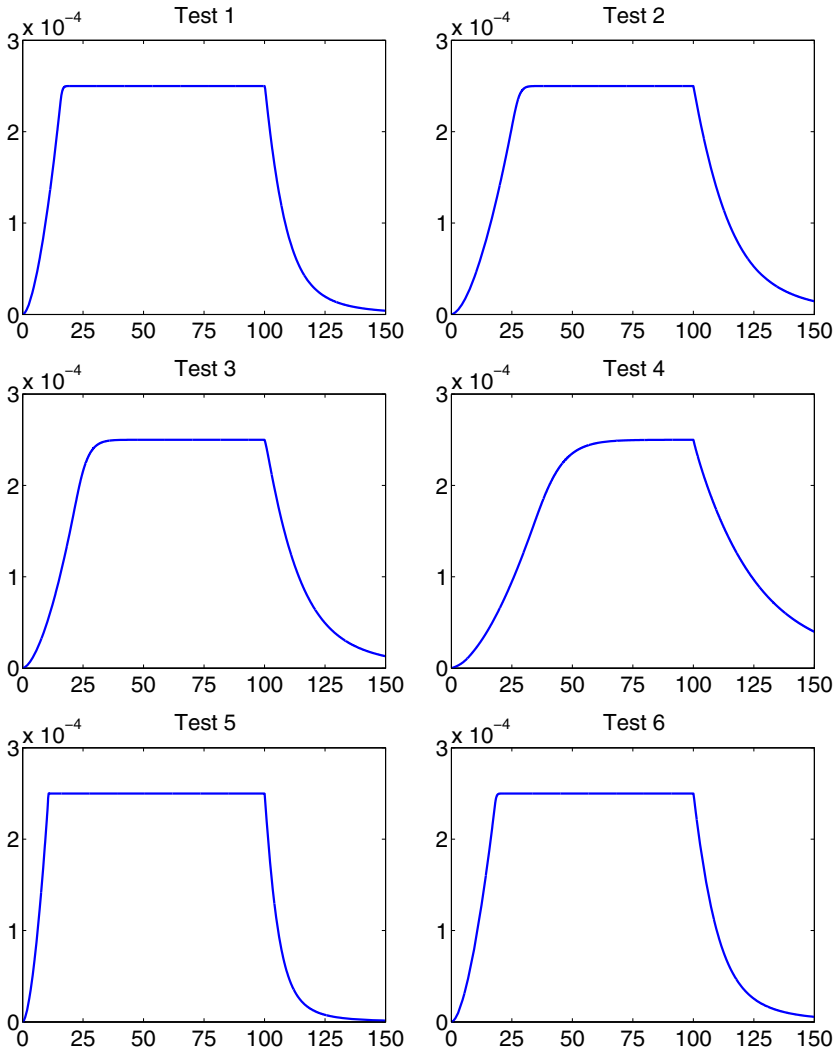

Figure 5. Example 3: Outlet discharge as a function of time. While comparing with the results in [24], the discharge values are to be multiplied by 0.2, which is the width of the 2-D computational domain in [24].

Example 4 – Convergence to a non-trivial equilibrium. In this example taken from [25], we simulate a subcritical flow over a nonflat bottom. As described in [25], the system (2.1) with $R(x,t) \equiv 0$, $n = 0.03$, and $g = 9.81$ admits the non-trivial steady-state solution with

$$h_{\mathrm{st}}(x) = 0.8 + \frac{1}{4}\exp\left[-\frac{135}{4}\left(\frac{x-75}{150}\right)^2\right], \quad q_{\mathrm{st}}(x) \equiv 2,$$

and the bottom topography function B satisfying

$$B'(x) = \left(\frac{4}{9.81\,h_{\mathrm{st}}^3(x)} - 1\right)h_{\mathrm{st}}'(x) - \frac{0.0036}{h_{\mathrm{st}}^{10/3}(x)}.$$

We prescribe zero initial condition ($h(x,0) \equiv q(x,0) \equiv 0$) throughout the computational domain $[0, 150]$ and implement the following boundary conditions by setting the ghost cell values to be

$$\overline{h}_0 := 2\overline{h}_1 - \overline{h}_2, \quad \overline{q}_0 := 2, \qquad \overline{h}_{N+1} := h_{\mathrm{st}}(x_{N+1}), \quad \overline{q}_{N+1} := \overline{q}_N.$$

DOI: 10.1002/fld

In addition, we fix the first component of inlet numerical flux by setting

$$H^{(1)}_{\frac{1}{2}} := 2$$

for all times.

The solution of the studied initial-boundary value problem is expected to converge to the aforementioned steady state as $t \to \infty$. We test our scheme on different grids varying the number of cells N from 50 to 1600 and study the convergence rate by comparing the computed solutions with the steady-state one at time $T_{\max} = 1200$. The solution (w and q) computed with $N = 50$ is plotted in Figure 6 together with the steady-state solution. As one can see, the proposed method captures the exact steady state quite accurately even on such a coarse grid (the obtained results are a little better than the one reported in [25]). When the mesh is refined, the second-order convergence rate is observed in h, while the q component converges with almost third order (Table III), where we show both the L^1-norm and L^∞-norm of the errors together with the experimental convergence rates.

Example 5 – Oscillating lake. We consider shallow water flow with wet/dry fronts in a frictional parabolic bottom. This example is a modification of the numerical example studied in [41, 42]: We use the same initial data and bottom topography function, but we replace the linear friction term used in [41, 42] with the Manning friction term. The main goal of this example is to study the impact of the small parameter ε in the desingularization procedure (3.10) on the computed solution.

We consider the bottom topography described by the function

$$B(x) = 10\left[\left(\frac{x}{3000}\right)^2 - 1\right],$$

and set the following initial conditions:

$$w(x,0) = \max\{k_1 x + k_2, B(x)\}, \quad q(x,0) \equiv 0,$$

where $k_1 = 0.0023660539018216433$ and $k_2 = -1.25959748992322$. We use the Manning friction term with the coefficient $n = 0.02$.

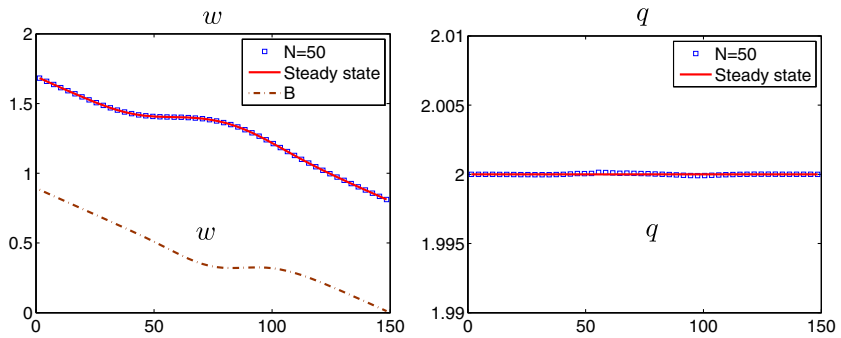

Figure 6. Example 4: Solution ($w(x, 1200)$ and $q(x, 1200)$) computed using $N = 50$ and the exact steady-state solution.

Table III. Example 4: The L^1-error and L^∞-error and convergence rates for h and q.

	h				q			
N	L^1-norm	Rate	L^∞-norm	Rate	L^1-norm	Rate	L^∞-norm	Rate
100	5.42E-03	––	1.53E-04	––	7.22E-04	––	1.66E-05	––
200	1.34E-03	2.017	3.78E-05	2.017	9.06E-05	2.993	2.10E-06	2.983
400	3.33E-04	2.010	9.39E-06	2.009	1.13E-05	2.998	2.62E-07	3.003
800	8.28E-05	2.005	2.34E-06	2.005	1.42E-06	2.999	3.28E-08	2.998
1600	2.07E-05	2.002	5.84E-06	2.002	1.79E-07	2.988	4.57E-09	2.843

DOI: 10.1002/fld

We run the simulation over the computation domain $[-5000, 5000]$, which is divided into $N = 1000$ cells. We use three different values of the desingularization parameter $\varepsilon = 10^{-4}$, 10^{-8}, and 10^{-12} and compute the solutions until the final time $t = 3000$. The snapshots of the computed solutions at $t = 300$, 1000, and 3000 are shown in Figure 7. As one can see, the solutions obtained with the different values of ε are almost indistinguishable. This clearly demonstrates that the proposed central-upwind scheme is not sensitive to the selection of ε.

Example 6 – Wet/dry front propagation over a V-shape bottom topography. In this example, we simulate a package of water released on the left part of a V-shape valley (Figure 8). The water steams down the left part and gradually accelerates. After passing the lowest point of the bottom, it starts climbing up the right slope, meanwhile gradually losing its speed. Before the water starts streaming down the right slope, the wet/dry front achieves its maximum height. Our goal is to study this front propagation quantitatively.

We consider a V-shape bottom topography function,

$$B(x) = \frac{1}{\sqrt{3}}\,|x-1|,$$

and take the friction coefficient $n = 0.02$. Initially, a package of water has a parabolic profile and zero velocity:

$$h(x,0) = \max\{0, -1.5(x-0.3)(x-0.7)\}, \quad q(x,0) \equiv 0.$$

We take a computational domain to be sufficiently large ($[0,2]$) so that the vibrating water body never reaches the boundaries.

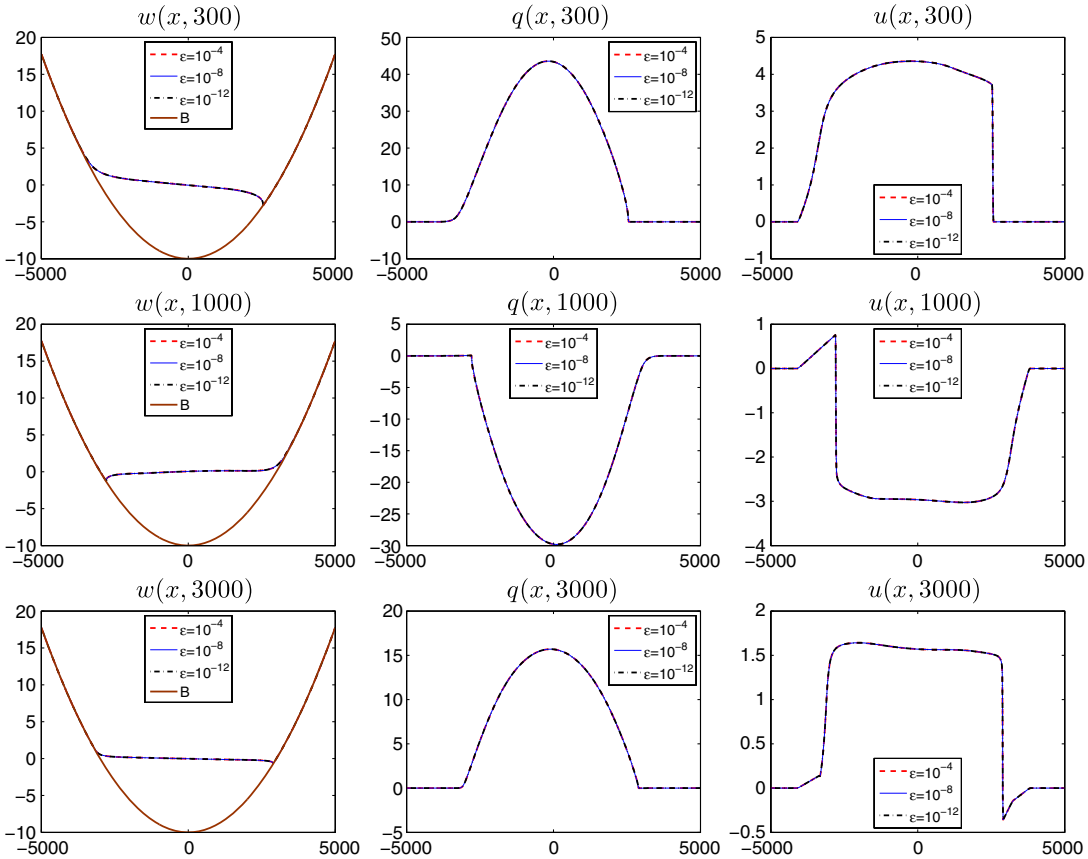

Figure 7. Example 5: Snapshots of w, q, and u computed with $\varepsilon = 10^{-4}$, 10^{-8}, and 10^{-12}.

DOI: 10.1002/fld

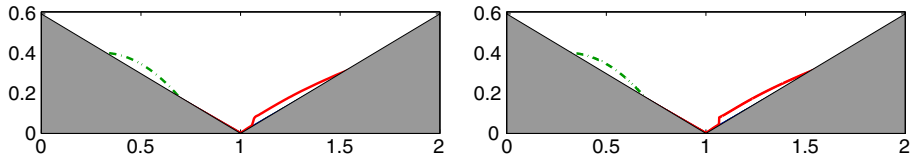

Figure 8. Example 6: Water profiles at $t = 0$ (dashed line) and $t = T_{\max}$ (solid line) computed with $N = 400$ (left) and 6400 (right).

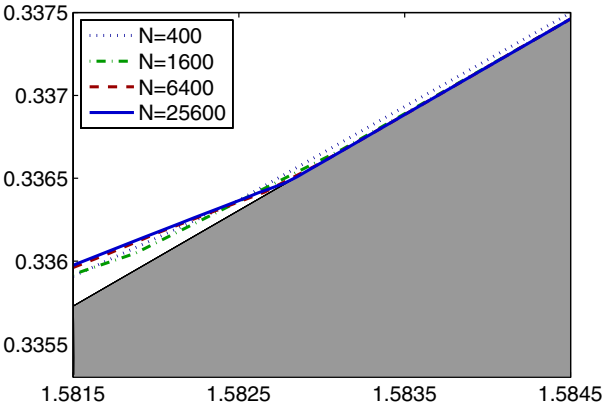

Figure 9. Example 6: Zoom at the wet/dry fronts of the computed and reference ($N = 25600$) solutions.

Table IV. Example 6: The L^1-errors and convergence rates for h and q.

	h		q	
N	L^1-error	Rate	L^1-error	Rate
100	1.40E-03	−−	9.13E-04	−−
200	5.24E-04	1.42	3.39E-04	1.43
400	2.00E-04	1.39	1.25E-05	1.44
800	9.47E-05	1.08	6.14E-05	1.02
1600	5.04E-05	0.91	3.75E-06	0.71
3200	2.26E-05	1.16	1.68E-06	1.16
6400	9.19E-06	1.30	6.63E-06	1.34

We run the computation on different grids varying the number of cells N from 100 to 6400 and compute a reference solution using $N = 25600$. According to the reference solution, the wet/dry front arrives at its highest point on the right slope at time $T_{\max} = 0.87839$. In Figure 8, we plot the water profile computed with $N = 400$ and 6400 at $t = 0$ and $t = T_{\max}$. Also, in Figure 9, we zoom at the wet/dry front area and compare the solutions computed using $N = 400$, 1600, and 6400 with the reference solution. Finally, in Table IV, we show the L^1-norm of the errors and compute the experimental convergence rates, which are slightly above 1. This rate is expected given the fact that the solution is not smooth.

4.2. *Two-dimensional examples*

Example 7 – Oscillating lake. Similar to the 1-D Example 5, we consider shallow water flow with a wet/dry front in a frictional parabolic bowl. This example is a modification of the oscillating lake example from [43]: as in the 1-D case, we replace the linear friction term with the nonlinear (Manning) one. Our goal is to demonstrate the ability of the proposed central-upwind scheme to accurately capture wet-dry fronts.

DOI: 10.1002/fld

Following [43], we take the parabolic bottom topography,

$$B(x,y)=\frac{1}{900000}(x^2+y^2),$$

and the following initial conditions:

$$w(x,y,0)=\max\{k_1x+k_2y+8.75,\,B(x,y)\},\ \ q(x,y,0)\equiv 0,\ \ p(x,y,0)=5(w(x,y,0)-B(x,y)),$$

where $k_1=0.002303379160180876$ and $k_2=0.0005$. We use the Manning friction term with the coefficient $n=0.02$.

We run the simulation until the final time $T_{max}=100$ in the computation domain $[-5000,5000]\times[-5000,5000]$, which is divided into $N\times N$ grid cells with $N=50$, 100, 200, 400, and 800. The fine mesh ($N=800$) solution is shown in Figure 10, where we show the computed water surface (w), water depth (h), as well as the discharges (q and p), and velocities (u and v). As one can see, the wet/dry front is quite sharply captured by the central-upwind scheme, and the velocities, which are computed using the desingularization procedure near the front, do not contain large spikes, and thus, the efficiency of the scheme is maintained.

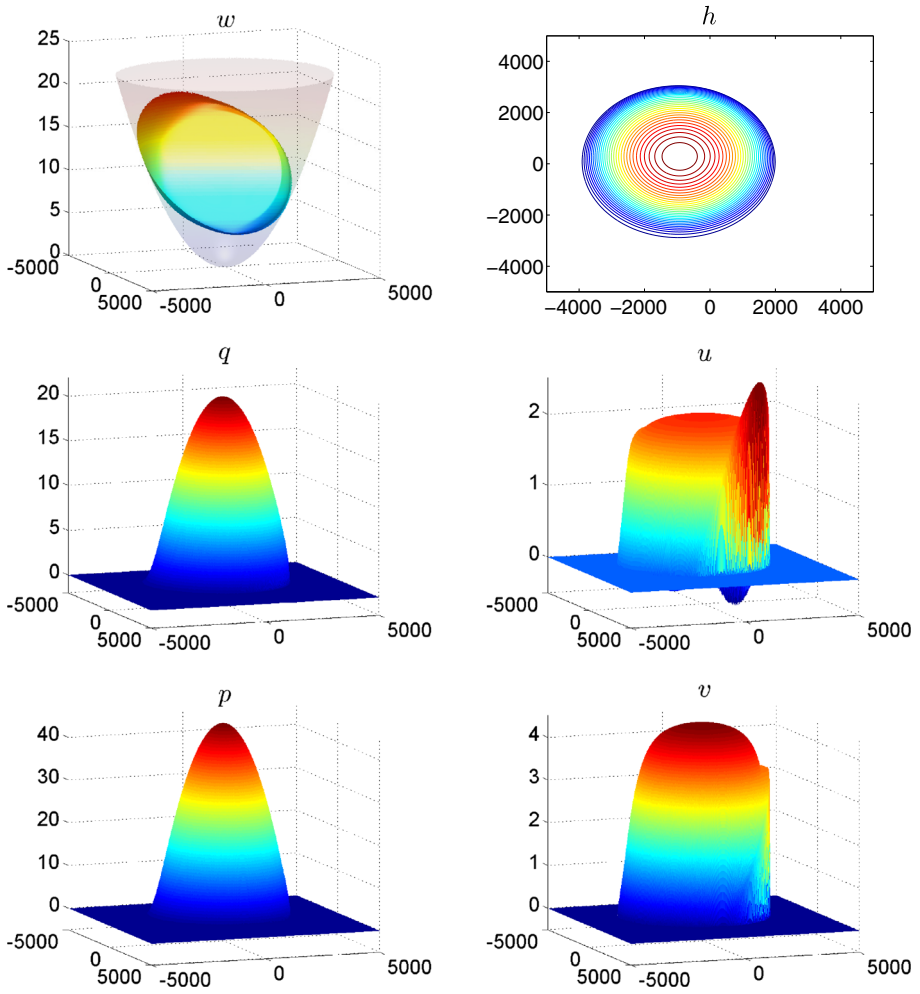

Figure 10. Example 7: Solution (w, h, q, u, p, and v) computed using the fine 800×800 grid.

DOI: 10.1002/fld

To verify the rates of convergence of the proposed method, we measure the difference between the solutions computed on two consecutive grids using the weighted L^1-differences, which are defined as follows:

$$\|\phi^N - \psi^N\|_1 := \frac{1}{N^2}\sum_{j=1}^{N}\sum_{k=1}^{N}|\phi^N_{j,k} - \psi^N_{j,k}|,$$

where $\phi^N := \{\phi^N_{j,k}\}$ and $\psi^N := \{\psi^N_{j,k}\}$ are two functions prescribed on the $N \times N$ grid. To apply this formula to the solutions computed on two different grids, we project the fine grid solution onto the coarse grid using the conservative projection. Then, to measure the experimental convergence rates r for h, we use the ratio of the weighted L^1-differences:

$$r = \log_2\left(\frac{\|h^{N/2} - h^{N/4}\|_1}{\|h^N - h^{N/2}\|_1}\right).$$

The rates for q and p are computed similarly.

The obtained results, reported in Table V, indicate that the experimental convergence rate of the proposed central-upwind scheme is slightly smaller than 2.

Example 8 – Rainfall runoff over an urban area. We consider another rainfall-runoff example, which now occurs over a more complicated 2-D surface containing houses as outlined in Figure 1 (right).

The setting corresponds to the laboratory experiment reported in [32]. The surface structure is shown in Figure 11. The experimental setting was built to mimic an urban area within the laboratory simulator of size 2 $\times$ 2.5 meters. To model urban buildings, several blocks were placed onto the surface according to different geometries, three of which are shown in Figure 11. In these three configurations, the houses are aligned in either the x-direction (Configuration X20), y-direction (Configuration Y20), or both (Configuration S20). The bottom topography function $B(x, y)$ is defined as

$$B(x,y) = \begin{cases} (x,y), & \text{outside the house region,} \\ \mathcal{H}(x,y;x_h,y_h), & \text{inside the house region centered at } (x_h,y_h). \end{cases}$$

Table V. Example 7: The weighted L^1-differences between the solutions computed on consecutive grids and the corresponding convergence rates.

N	$\|h^N - h^{N/2}\|_1$	Rate	$\|q^N - q^{N/2}\|_1$	Rate	$\|p^N - p^{N/2}\|_1$	Rate
100	9.35E-03	––	2.56E-02	––	3.73E-02	––
200	2.72E-03	1.782	7.75E-03	1.724	9.98E-03	1.903
400	8.41E-04	1.694	2.42E-03	1.682	2.74E-03	1.864
800	2.63E-04	1.675	7.20E-04	1.745	7.73E-04	1.825

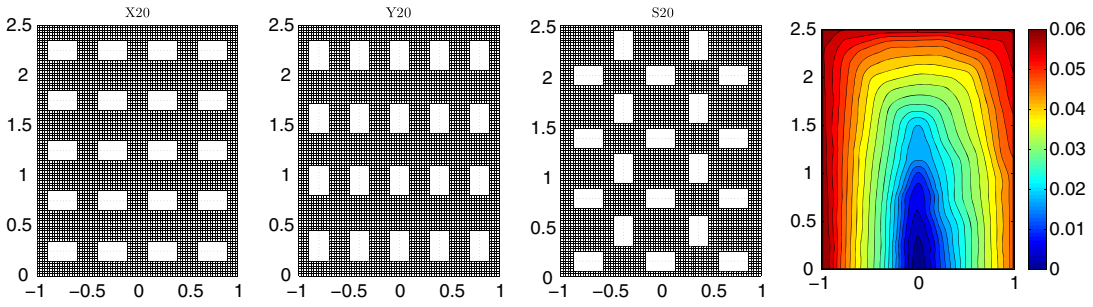

Figure 11. Example 8: Three house configurations (X20 ,Y20, and S20) and contour plot of the urban area structure $\mathcal{S}$. In each configuration, the houses are placed in the blank rectangles such that the house ridges coincide with the dotted lines.

DOI: 10.1002/fld

The precise data of the surface structure $\mathcal{S}(x,y)$ were provided by Dr. Luis Cea, and the house-roof configuration $\mathcal{H}(x,y;x_h,y_h)$ was computed according to the following formulae:

$$\mathcal{H}(x,y;x_h,y_h)=\begin{cases}0.3-|y-y_h|, & (x,y)\in[x_h-0.15,x_h+0.15]\times[y_h-0.1,y_h+0.1],\\ 0, & \text{otherwise},\end{cases}$$

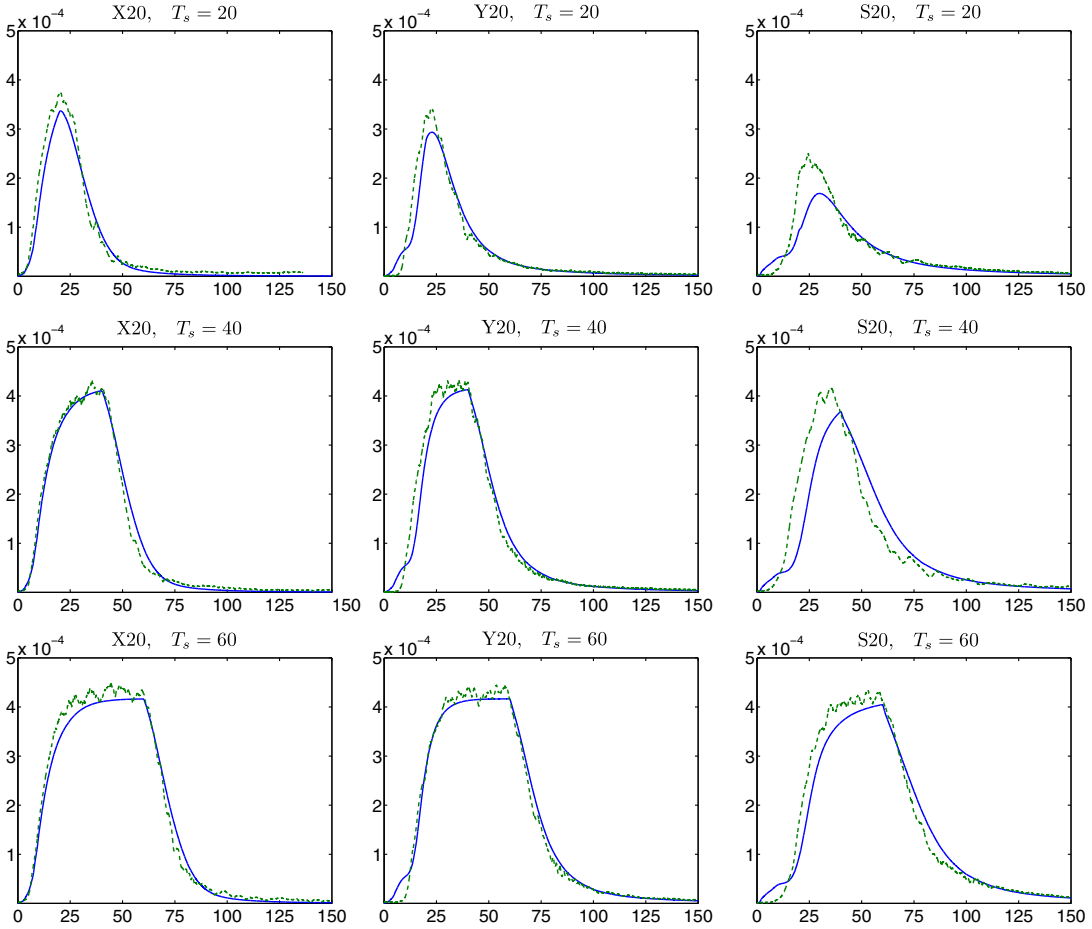

Figure 12. Example 8: Outlet discharge (the experimental data, dashed line, versus the computed results, solid line) as a function of time.

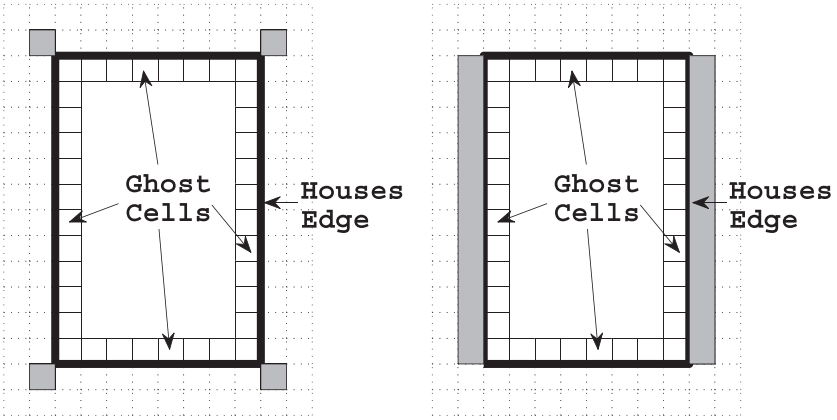

Figure 13. Example 8a: Special treatment of a house region. The house edges are considered to be a part of an internal boundary. The rainfall on the roof is uniformly distributed into the shaded cells. There are two cases: the one with the gutter system installed (left) and the one without such a system (right).

DOI: 10.1002/fld

for houses aligned in x-direction and

$$\mathcal{H}(x,y;x_h,y_h)=\begin{cases}0.3-|x-x_h|, & (x,y)\in[x_h-0.1,x_h+0.1]\times[y_h-0.15,y_h+0.15],\\ 0, & \text{otherwise},\end{cases}$$

for houses aligned in y-direction. Notice that across the walls of the houses, the bottom topography is discontinuous, and thus, the bilinear interpolant (3.17) has very sharp gradients there.

Similarly, to the 1-D rainfall-runoff example, we set the following almost dry initial conditions:

$$h(x,y,0)\equiv 0,\quad q(x,y,0)\equiv 0,\quad p(x,y,0)\equiv 0.$$

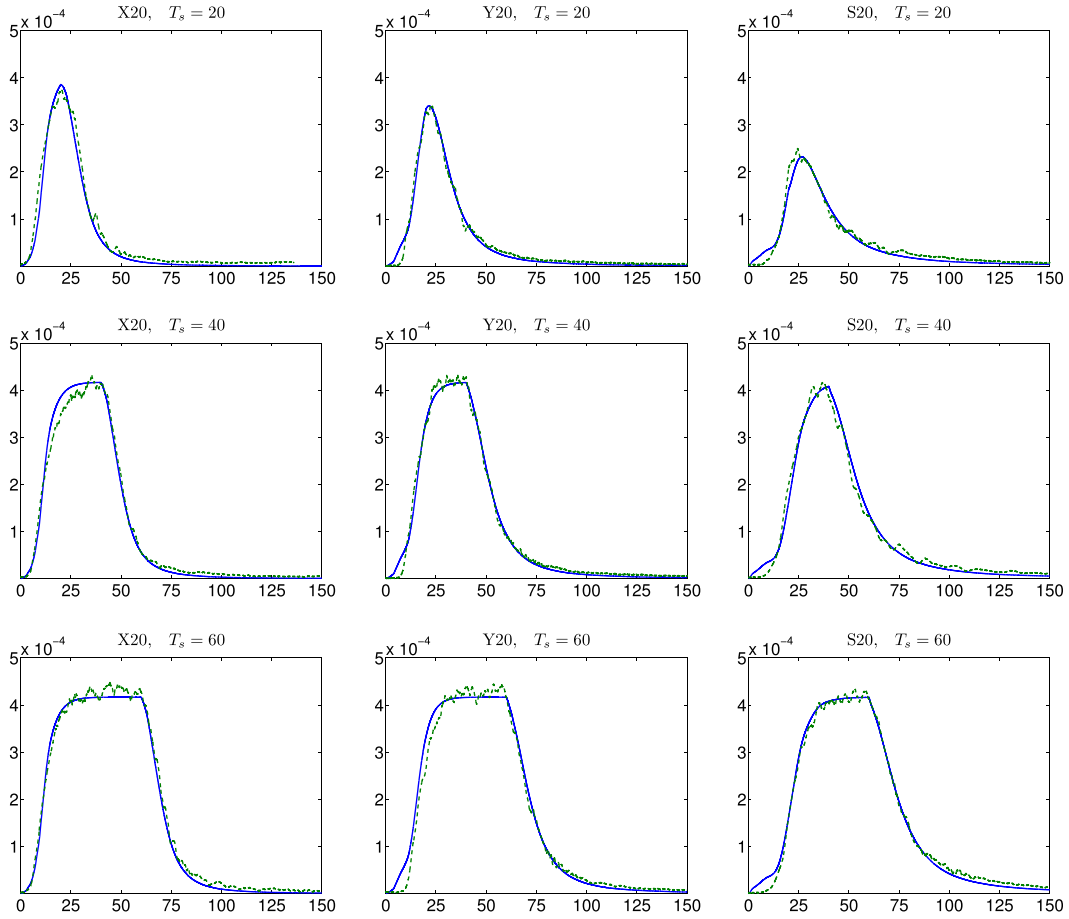

Figure 14. Example 8a: Outlet discharge (the experimental data, solid line, versus the computed results, dashed line) as a function of time.

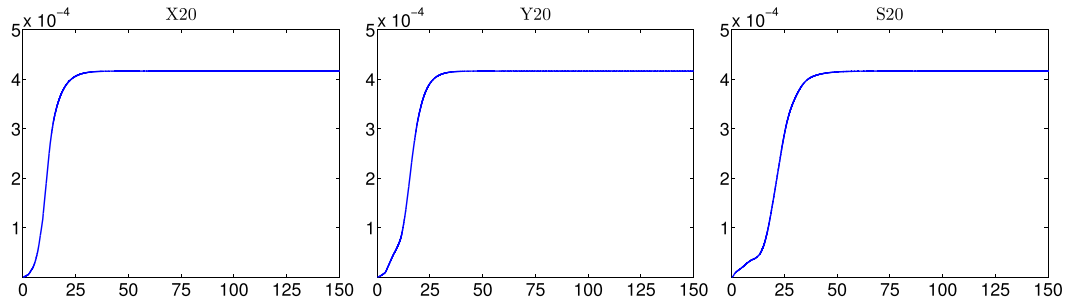

Figure 15. Example 8a: Outlet discharge as a function of time: convergence to a steady state when the rain source is not switched off.

DOI: 10.1002/fld

The rain of a constant intensity starts falling at time $t = 0$ and stops at $t = T_s$, that is,

$$R(x, y, t) = \begin{cases} \dfrac{1}{12000}, & 0 \leqslant t \leqslant T_s, \\ 0, & \text{otherwise.} \end{cases}$$

In different experiments, different values of $T_s = 20, 40, 60$, or ∞ have been used. The computational domain $[-1, 1] \times [0, 2.5]$ is divided into $N_x \times N_y$ uniform cells (we have taken $N_x = 80$ and $N_y = 100$). The solid wall boundary conditions have been set at the left, right, and top parts of the boundary, while absorbing boundary conditions have been implemented at the lower part ($-1 \leqslant x \leqslant 1$, $y = 0$). As in the 1-D case, we use the ghost cell technique, and the ghost cell values are set to be

$$\overline{h}_{j,0} := 0, \quad \overline{q}_{j,0} := 0, \quad \overline{p}_{j,0} := 0, \quad j = 1, \ldots, N_x.$$

At this boundary, the total outlet discharge is computed using $\Delta y \sum_{j=1}^{N_x} \left(H^y_{j,1/2}\right)^{(1)}$.

In Figure 12, the outlet discharge is plotted as a function of time and compared with the experimental data provided to us by Dr. Luis Cea. Notice that in some cases (for example, for Configuration Y20 with $T_s = 20$ or 40 and Configuration S20), the computed curves have lower peaks than the experimental ones. We believe that such a delay of outlet discharge can be explained by inability of the system (1.2)–(1.4) to accurately model the situation occurring near the house walls where the size of the jumps in the bottom topography is about 2-3 orders of magnitude larger than the water depth. We therefore modify the model by removing the houses from the computational domain and placing the entire rainwater, which would accumulate over the houses, near the house walls inside the computational domain. The details of a modified approach are given in Example 8a.

Example 8a – Modified house treatment. We consider the same setting as in Example 8, but make the following modifications.

First, we remove the houses from the computational domain, which becomes a punctured rectangle. A typical hole is depicted in Figure 13: The house walls become the internal boundary, which is numerically treated using the solid wall ghost cell technique. Second, we redistribute the rainwater falling onto the roof so that it is placed inside the modified computational domain. In the laboratory experiment, the water falling on the house blocks streams down from the long (lower) edges and finally joins the surface water flow, while in reality, the gutter system is commonly used and the rainwater streams down from the rain pipes typically located at the house corners.

In the numerical experiments, we adopt two different strategies to mimic the aforementioned two draining situations. In both cases, the building-roof rainfall is uniformly distributed on certain cells

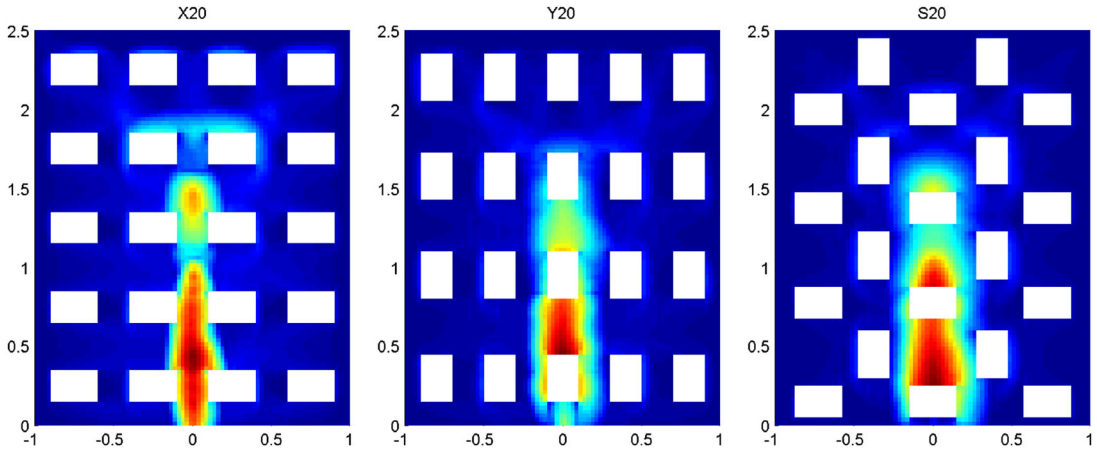

Figure 16. Example 8a: Water height snapshots at the steady state achieved when the rain source is not switched off.

DOI: 10.1002/fld

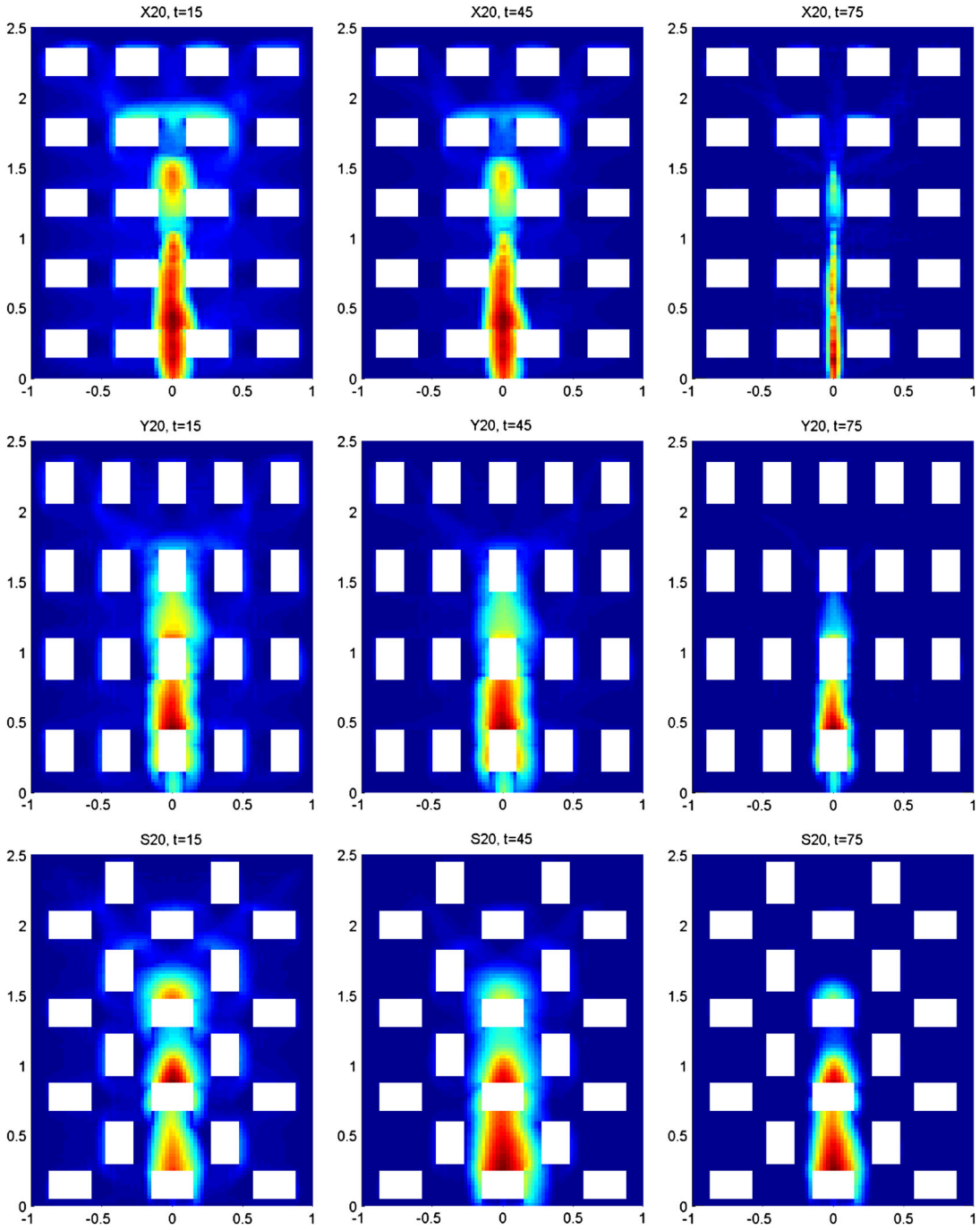

Figure 17. Example 8a: Water height snapshots at times $t = 15$, 45, and 75 computed for Configurations X20, Y20, and S20 with $T_s = 40$.

near and outside the building edges. These are the shaded cells in Figure 13. The modified rain source can then be written as follows:

$$\widehat{R}(x, y, t) = \begin{cases} \dfrac{1}{12000}\left(1 + \dfrac{A_{\mathrm{h}}}{A_{\mathrm{s}}}\right), & \text{in the shaded cells,} \\ \dfrac{1}{12000}, & \text{otherwise,} \end{cases}$$

DOI: 10.1002/fld

which is, as before, switched on only for $t \in [0, T_s]$. Here, A_{h} is the area of the house, and A_{s} is the area of the shaded region near that house. If the gutter system is installed, then in all studied configurations (X20, Y20, and S20) with $N_x = 80$ and $N_y = 100$, we have

$$\frac{A_{\mathrm{h}}}{A_{\mathrm{s}}} = \frac{0.2 \cdot 0.3}{4\Delta x \Delta y} = 24.$$

If the gutter system is not installed, then this ratio depends on a house orientation, but since in this numerical example, we take $\Delta x = \Delta y = 1/40$, then

$$\frac{A_{\mathrm{h}}}{A_{\mathrm{s}}} = \frac{0.2 \cdot 0.3}{2 \cdot 0.3\Delta x} = \frac{0.2 \cdot 0.3}{2 \cdot 0.3\Delta y} = 4$$

for all of the configurations (X20, Y20, and S20).

Again, we compare the outlet discharges obtained by our numerical scheme and the laboratory measurement. As we can see in Figure 14, our numerical results are now in much better agreement with the experimental results, especially for Configurations Y20 (with $T_s = 20$ and 40) and S20. In other cases, the achieved resolution is also slightly higher, though the improvement is not so essential. It should also be observed that in the case of a longer rain duration ($T_s = 60$), the computed outlet discharge remains almost constant for $t \in [30, 60]$ for Configurations X20 and Y20. In fact, if the rain source is not switched off ($T_s = \infty$), the outlet discharge will converge to a steady state as shown in Figure 15. The snapshots of a water height at this steady state are shown in Figure 16.

Finally, in Figure 17, we plot time snapshots of the water height obtained for Configurations X20, Y20, and S20 (we now use $T_s = 40$). The graphs illustrate how the rainwater drains and clarify the dependence of the water flow on the surface configuration. In the examples using Configuration X20, the draining stream takes advantage of the space along the vertical central line $x = 0$ and a big mainstream is formed. In the examples using Configurations Y20 and S20, there are houses on the central line $x = 0$ that block the flow there. Therefore, the mainstream of draining water has to bypass these houses, and thus, small 'lakes' are developed behind two of the houses, see Configurations Y20 and S20 in Figure 17. This explains why the total amount of water flew out of the domain may not be the same as in the measured data because in the experimental setting, the 'lakes' drain through the gaps between the building blocks and the bottom surface.

Remark 4.2

We would like to point out that the aforementioned two different strategies of modifying the rain source term near the houses lead to practically the same results. In the reported numerical

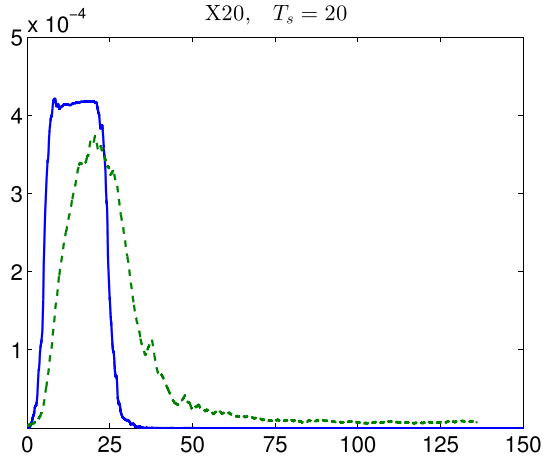

Figure 18. Example 8a: Significance of the bottom friction. The solid line is the measured outlet discharge for Configuration X20 with $T_s = 20$; the dashed line is the numerical outlet discharge for the same example computed using the frictionless system (1.1).

DOI: 10.1002/fld

experiments, we have redistributed the rain falling onto the house into the cells along the longer house edges (Figure 13, right) as discussed in the beginning of Example 8a.

Remark 4.3
Another point, we would like to clarify the necessity of including the bottom friction terms in the studied shallow water model. In Figure 18, we compare the measured data with the numerical result obtained by solving the frictionless system (1.1). In this case, the computed outlet discharge changes dramatically even when the simplest Configuration X20 with $T_s = 20$ is considered.

5. CONCLUSION

We have studied the shallow water system with friction terms and developed a positivity preserving semi-discrete central-upwind scheme, which is well-balanced in the sense that it is capable of exactly preserving special types of steady-state solutions: both the 'lake-at rest' and 'slanted surface' ones. Because of the presence of friction terms, the ODE system arising from the central-upwind semi-discretization becomes stiff, and therefore, we have implemented an efficient semi-implicit Runge-Kutta time integration method that sustains the well-balanced and sign preserving properties of the semi-discrete scheme. We have tested the performance of the new method in a number of 1-D and 2-D examples, including Example 8, which focuses on modeling the rainwater drainage in urban areas that contain houses. Since the rainwater depth is typically several orders of magnitude smaller than the height of the houses, a direct application of the shallow water equations leads to a substantial discrepancy between the numerical and experimental results. We therefore have developed a special technique, according to which the houses are removed from the computational domain while the rainwater is redistributed into the nearby areas. The new technique helps to achieve a remarkable agreement between the numerical and experimental results.

ACKNOWLEDGMENT

The work of A. Chertock was supported in part by the NSF Grant DMS-1216974 and the ONR Grant N00014-12-1-0832. The work of A. Kurganov was supported in part by the NSF Grant DMS-1216957 and the ONR Grant N00014-12-1-0833. The work of S. Cui was supported in part by NSF Grants DMS-1115718 and DMS-1216957. The work of T. Wu was supported in part by the NSF Grants DMS-1115718 and DMS-1216957. A part of this research was conducted during the summers of 2012 and 2013, when the authors visited the Institute of Natural Sciences at the Shanghai Jiao Tong University, China. The authors would like to thank the faculty, staff, and especially the Institute co-director Prof. Shi Jin for their support and hospitality. The authors also thank Dr. Mario Ricchiuto for encouraging discussions. The authors are thankful to Dr. Luis Cea for providing the experimental data and for his help.

REFERENCES

1. de Saint-Venant AJC. Thèorie du mouvement non-permanent des eaux, avec application aux crues des rivière at à l'introduction des marèes dans leur lit. *Comptes Rendus de L'Académie des Sciences* 1871; **73**:147–154.
2. Audusse E, Bouchut F, Bristeau M-O, Klein R, Perthame B. A fast and stable well-balanced scheme with hydrostatic reconstruction for shallow water flows. *SIAM Journal on Scientific Computing* 2004; **25**:2050–2065.
3. Bollermann A, Chen G, Kurganov A, Noelle S. A well-balanced reconstruction for wet/dry fronts. *Journal of Scientific Computing* 2013; **56**:267–290.
4. Bollermann A, Noelle S, Lukáčová-Medvid'ová M. Finite volume evolution Galerkin methods for the shallow water equations with dry beds. *Communications in Computational Physics* 2011; **10**(2):371–404.
5. Bryson S, Epshteyn Y, Kurganov A, Petrova G. Well-balanced positivity preserving central-upwind scheme on triangular grids for the Saint-Venant system. *ESAIM: Mathematical Modelling and Numerical Analysis* 2011; **45**(3): 423–446.
6. Gallardo JM, Parés C, Castro M. On a well-balanced high-order finite volume scheme for shallow water equations with topography and dry areas. *Journal of Computational Physics* 2007; **227**(1):574–601.
7. Jin S, Wen X. Two interface-type numerical methods for computing hyperbolic systems with geometrical source terms having concentrations. *SIAM Journal on Scientific Computing* 2005; **26**(6):2079–2101.

DOI: 10.1002/fld

8. Kurganov A, Levy D. Central-upwind schemes for the saint-venant system. *ESAIM: Mathematical Modelling and Numerical Analysis* 2002; **36**:397–425.
9. Kurganov A, Petrova G. A second-order well-balanced positivity preserving central-upwind scheme for the saint-venant system. *Communications in Mathematical Sciences* 2007; **5**:133–160.
10. LeVeque RJ. Balancing source terms and flux gradients in high-resolution Godunov methods: the quasi-steady wave-propagation algorithm. *Journal of Computational Physics* 1998; **146**(1):346–365.
11. Noelle Sebastian, Xing Yulong, Shu Chi-Wang. High-order well-balanced schemes, Numerical Methods for Balance Laws, 2009; 1–66.
12. Perthame B, Simeoni C. A kinetic scheme for the Saint-Venant system with a source term. *Calcolo* 2001; **38**(4): 201–231.
13. Ricchiuto M, Bollermann A. Stabilized residual distribution for shallow water simulations. *Journal of Computational Physics* 2009; **228**(4):1071–1115.
14. Rogers B, Fujihara M, Borthwick A G L. Adaptive Q-tree Godunov-type scheme for shallow water equations. *International Journal for Numerical Methods in Fluids* 2001; **35**(3):247–280.
15. Russo G, Khe A. High order well balanced schemes for systems of balance laws. In *Hyperbolic Problems: Theory, Numerics and Applications*, vol. 67, Proc. Sympos. Appl. Math. Amer. Math. Soc.: Providence, RI, 2009; 919–928.
16. Russo G, Khe A. High order well-balanced schemes based on numerical reconstruction of the equilibrium variables. *Proceedings "WASCOM 2009" 15th Conference on Waves and Stability in Continuous Media*, World Sci. Publ., Hackensack, NJ, 2010; 230–241.
17. Xing Y, Shu C-W, Noelle S. On the advantage of well-balanced schemes for moving-water equilibria of the shallow water equations. *Journal of Scientific Computing* 2011; **48**(1–3):339–349.
18. Gerbeau J-F, Perthame B. Derivation of viscous Saint-Venant system for laminar shallow water; numerical validation. *Discrete and Continuous Dynamical Systems - Series B* 2001; **1**(1):89–102.
19. Kellerhals R. Stable channels with gravel-paved beds. *ASCE Journal of the Waterways and Harbors Division* 1967; **93**(1):63–84.
20. Flamant A. *Mécanique Appliquée : Hydraulique*. Baudry éditeur: Paris, France, 1891.
21. Darcy H. *Recherches expérimentales Relatives au mouvement de l'eau dans les tuyaux*, Vol. 1. Mallet-Bachelier: Paris, 1857.
22. Gauckler Ph. *Etudes théoriques et pratiques sur l'ecoulement et le mouvement des eaux*. Gauthier-Villars: Paris, 1867.
23. Manning R. On the flow of water in open channel and pipes. *Transactions of the Institution of Civil Engineers of Ireland* 1891; **20**:161–207.
24. Cea L, Vázquez-Cendón M E. Unstructured finite volume discretisation of bed friction and convective flux in solute transport models linked to the shallow water equations. *Journal of Computational Physics* 2012; **231**(8):3317–3339.
25. Berthon C, Marche F, Turpault R. An efficient scheme on wet/dry transitions for shallow water equations with friction. *Computers & Fluids* 2011; **48**:192–201.
26. Kurganov A, Lin C-T. On the reduction of numerical dissipation in central-upwind schemes. *Communications in Computational Physics* 2007; **2**:141–163.
27. Kurganov A, Noelle S, Petrova G. Semi-discrete central-upwind scheme for hyperbolic conservation laws and Hamilton-Jacobi equations. *SIAM Journal on Scientific Computing* 2001; **23**:707–740.
28. Kurganov A, Tadmor E. New high resolution central schemes for nonlinear conservation laws and convection-diffusion equations. *Journal of Computational Physics* 2000; **160**:241–282.
29. Kurganov A, Tadmor E. Solution of two-dimensional Riemann problems for gas dynamics without Riemann problem solvers. *Numerical Methods for Partial Differential Equations* 2002; **18**:584–608.
30. Kurganov A, Petrova G. Central-upwind schemes for two-layer shallow equations. *SIAM Journal on Scientific Computing* 2009; **31**:1742–1773.
31. Chertock A, Cui S, Kurganov A, Tong W. Steady state and sign preserving semi-implicit Runge-Kutta methods for ODEs with stiff damping term. Submitted.
32. Cea L, Garrido M, Puertas J. Experimental validation of two-dimensional depth-averaged models for forecasting rainfall–runoff from precipitation data in urban areas. *Journal of Hydrology* 2010; **382**:88–102.
33. Gottlieb S, Ketcheson D, Shu C.-W. *Strong Stability Preserving Runge-Kutta and Multistep Time Discretizations*. World Scientific Publishing Co. Pte. Ltd.: Hackensack, NJ, 2011.
34. Gottlieb S, Shu C.-W., Tadmor E. Strong stability-preserving high-order time discretization methods. *SIAM Review* 2001; **43**:89–112.
35. Ascher UM, Ruuth SJ, Spiteri RJ. Implicit-explicit Runge-Kutta methods for time-dependent partial differential equations. *Applied Numerical Mathematics* 1997; **25**(2–3):151–167. Special issue on time integration (Amsterdam, 1996).
36. Higueras I, Roldán T. Positivity-preserving and entropy-decaying IMEX methods. In *Ninth International Conference Zaragoza-Pau on Applied Mathematics and Statistics*, vol. 33, Monogr. Semin. Mat. García Galdeano. Prensas Univ. Zaragoza: Zaragoza, 2006; 129–136.
37. Hundsdorfer W, Ruuth S J. IMEX extensions of linear multistep methods with general monotonicity and boundedness properties. *Journal of Computational Physics* 2007; **225**(2):2016–2042.
38. Higueras I, Happenhofer N, Koch O, Kupka F. Optimized strong stability preserving IMEX Runge–Kutta methods. *Journal of Computational and Applied Mathematics* 2014; **272**:116–140.

DOI: 10.1002/fld

39. Pareschi L, Russo G. Implicit-Explicit Runge-Kutta schemes and applications to hyperbolic systems with relaxation. *Journal of Scientific Computing* 2005; **25**:129–155.
40. Pareschi L, Russo G. Implicit-explicit Runge-Kutta schemes for stiff systems of differential equations. In *Recent Trends in Numerical Analysis*, vol. 3, Adv. Theory Comput. Math. Nova Sci. Publ.: Huntington, NY, 2001; 269–288.
41. Sampson J, Easton A, Singh M. Moving boundary shallow water flow above parabolic bottom topography. *The ANZIAM Journal* 2005; **47**((C)):C373–C387.
42. Sampson J, Easton A, Singh M. Moving boundary shallow water flow in a region with quadratic bathymetry. *The ANZIAM Journal* 2007/08; **49**((C)):C666–C680.
43. Hou J, Liang Q, Simons F, Hinkelmann R. A stable 2D unstructured shallow flow model for simulations of wetting and drying over rough terrains. *Computers & Fluids* 2013; **82**:132–147.

DOI: 10.1002/fld